Conjunctive changes in two distinct ion channels mediate activity-dependent intrinsic plasticity in rat dentate gyrus granule cells

Poonam Mishra and Rishikesh Narayanan*

Cellular Neurophysiology Laboratory, Molecular Biophysics Unit, Indian Institute of Science, Bangalore 560012, India.

*Corresponding author:

Rishikesh Narayanan, Ph.D.,
Molecular Biophysics Unit,
Indian Institute of Science,
Bangalore 560 012, India.
e-mail: rishi@iisc.ac.in
Phone: +91-80-22933372

Abbreviated title: Intrinsic plasticity in dentate gyrus granule cells

Keywords: engram cells; HCN channels; hippocampus; intrinsic excitability; plasticity manifold; persistent sodium channels

Author contributions
P. M. and R. N. designed experiments; P. M. performed experiments and carried out data analysis; P. M. and R. N. co-wrote the paper.

Competing financial interests
The authors declare no conflict of interest.

Acknowledgments

This work was supported by the Wellcome Trust-DBT India Alliance (Senior fellowship to RN; IA/S/16/2/502727), Human Frontier Science Program (HFSP) Organization (RN), the Department of Biotechnology through the DBT-IISc partnership program (RN), the Revati & Satya Nadham Atluri Chair at IISc (RN), the Department of Science and Technology (RN), and the Ministry of Human Resource Development (RN & PM). The authors thank Dr. Daniel Johnston, Dr. Sufyan Ashhad and the members of the cellular neurophysiology laboratory for helpful discussions and for comments on a draft of this manuscript.

SUMMARY

The concomitant roles of synaptic plasticity and neuron-specific intrinsic plasticity as putative cellular substrates of learning and memory are well established. Although the dentate gyrus (DG) was the first brain region to provide us electrophysiological insights about plasticity in synaptic strength and in intrinsic excitability, the assessment of the protocols, mechanisms and implications associated with intrinsic plasticity in DG has been surprisingly limited. In this study, we focused on identifying behaviorally relevant activity patterns that could induce intrinsic plasticity in granule cells (GC) and on mechanistically understanding such plasticity. We employed whole-cell patch-clamp recordings to explore the impact of intracellularly initiated theta-modulated burst firing, in the absence of synaptic stimulation, on neuronal intrinsic properties of rat GCs. We found that theta burst firing induced a significant reduction in sub-threshold excitability and temporal summation, accompanied by an unexpected contrasting enhancement of supra-threshold excitability in GCs. We show that conjunctive changes in HCN and persistent sodium channels mediated this form of plasticity, which was found to be dependent on influx of cytosolic calcium, with *L*-type calcium channels and intracellular calcium stores contributing to calcium influx. Our results unveil the expression of conjunctive plasticity in multiple channels, responding to the same activity pattern, thereby establishing a *plasticity manifold* involving strong rules governing concomitant plasticity in different components. We postulate that activity-dependent increase in neuronal firing rate could act as a putative substrate for the emergence of engram cells, and the associated reduction in sub-threshold excitability could concomitantly provide homeostatic balance and specificity to this encoding process.

INTRODUCTION

The concomitant roles of synaptic plasticity and neuron-specific intrinsic plasticity as putative cellular substrates of learning and memory are well established (Zhang and Linden, 2003; Kim and Linden, 2007; Johnston and Narayanan, 2008; Nelson and Turrigiano, 2008; Neves et al., 2008; Mozzachiodi and Byrne, 2010; Mayford et al., 2012; Narayanan and Johnston, 2012; Titley et al., 2017; Lisman et al., 2018; Rathour and Narayanan, 2019). The DG has been implicated in spatial navigation, response decorrelation, pattern separation, engram formation, learning and memory (Bliss and Lomo, 1973; Amaral et al., 2007; Leutgeb et al., 2007; McHugh et al., 2007; Bakker et al., 2008; Sahay et al., 2011; Aimone et al., 2014; Neunuebel and Knierim, 2014; Kropff et al., 2015; Diamantaki et al., 2016; Heigele et al., 2016; Danielson et al., 2017; GoodSmith et al., 2017; Li et al., 2017; Senzai and Buzsaki, 2017; Tonegawa et al., 2018; Mishra and Narayanan, 2019). The mechanisms behind and implications for synaptic plasticity to these physiological roles of the DG have been thoroughly investigated (Bliss and Lomo, 1973; Schmidt-Hieber et al., 2004; Govindarajan et al., 2006; McHugh et al., 2007; Aimone et al., 2014; Tonegawa et al., 2018). In contrast, the assessment of the protocols, mechanisms and implications associated with plasticity of intrinsic neuronal properties in the DG has been surprisingly limited (Lopez-Rojas et al., 2016; Titley et al., 2017). This lacuna is especially striking because the first ever report of long-term potentiation (which was in the DG) also had reported a concomitant increase in granule cell excitability (Bliss and Lomo, 1973), and because of prominent encoding roles for DG neurons as engram cells that could recruit neuron-specific changes to excitability (Titley et al., 2017).

Here, seeking to fill this lacuna, we focused on identifying behaviorally relevant activity patterns that could induce intrinsic plasticity in DG granule cells and on mechanistically

understanding such plasticity. In search of behaviorally relevant activity patterns, we first noted that theta frequency (4–10 Hz) oscillations are widely prevalent in the DG (Winson, 1974, 1978; Sainsbury and Bland, 1981; Bland, 1986; Buzsaki, 2002; Colgin, 2013, 2016) and granule cells exhibit theta-modulated bursts (Pernia-Andrade and Jonas, 2014). Although the impact of theta patterned stimuli has been widely studied with reference to synaptic plasticity (Greenstein et al., 1988; Pavlides et al., 1988; Shors and Dryver, 1994; Beck et al., 2000; Davis et al., 2004; McHugh et al., 2007; Larson and Munkacsy, 2015), the impact of theta burst firing in eliciting plasticity in *neuronal intrinsic properties* has not been explored. Therefore, employing whole-cell patch-clamp recordings, we explored the impact of intracellularly initiated theta-modulated burst firing, in the absence of synaptic stimulation, on intrinsic neuronal properties of DG granule cells.

We found that theta burst firing (TBF) induced a significant reduction in sub-threshold excitability and temporal summation, and an unexpected contrasting enhancement of supra-threshold excitability of DG granule cells. We provide strong lines of evidence, based on systematic analyses of signature electrophysiological characteristics and on results of experiments involving pharmacological agents, in support of conjunctive changes in HCN and persistent sodium channels mediating this form of plasticity. Finally, we demonstrated that TBF-induced intrinsic plasticity was dependent on influx of cytosolic calcium, with *L*-type calcium channels and intracellular calcium stores contributing to calcium influx. Our results unveil the expression of conjunctive plasticity in multiple channels, responding to the *same* activity pattern, thereby establishing a *plasticity manifold* involving strong rules governing concomitant plasticity in different components. Such a plasticity manifold ensures that neural components have specific rules associated with how expression of plasticity in these components is co-regulated, thereby

providing a molecular substrate for neurons to traverse across different stable states (say, each *encoding* different contexts without altering activity *homeostasis*) within the neuronal intrinsic manifold (Jazayeri and Afraz, 2017; Krakauer et al., 2017; Rathour and Narayanan, 2019). We postulate that the activity-dependent increase in neuronal firing rate could act as a putative substrate for the emergence of engram cells, and the associated reduction in sub-threshold excitability could concomitantly provide homeostatic balance to the encoding process.

RESULTS

We performed whole-cell current clamp recordings from the somata of granule cells in the dentate gyrus. The behaviorally relevant activity pattern that we explored in our analyses is theta-burst firing (TBF), initiated by theta-patterned supra-threshold current injections (Fig. 1*C*, bottom) to induce AP bursts (Fig. 1*C*, top). We first asked if intrinsic properties of DG granule cells change in response to behaviorally relevant activity patterns. We recorded several sub- and supra-threshold measurements before and after TBF induction to monitor changes in various intrinsic properties of granule cell (Table 1).

Theta burst firing elicited contrasting patterns of plasticity in sub- *vs.* supra-threshold physiological properties of granule cells.

We found a significant long-term decrease in input resistance of GC post-TBF that persisted for more than 40 mins (Fig. 1*D*, Fig. 2*A–C*). The membrane potential also depolarized (~7 mV) through this period, but all measurements were obtained at the initial RMP to avoid confounds because of altered driving forces to different ion channels (Fan et al., 2005; Narayanan and Johnston, 2007, 2008; Narayanan et al., 2010; Brager et al., 2012; Clemens and Johnston, 2014; Mishra and Narayanan, 2015; Malik and Johnston, 2017). Consistent with the reduction in R_{in}, we also found a concomitant persistent reduction in impedance amplitude (Fig. 1*E–F*), which was quantified using maximal impedance amplitude ($|Z|_{max}$; Fig. 2*D–E*), and in temporal summation (Fig. 1*G*, Fig. 2*G*) measured from the neuron's response to five alpha excitatory postsynaptic currents. Despite these reductions in subthreshold excitability measurements, which should have typically resulted in reduced AP firing (Fan et al., 2005; Narayanan and Johnston, 2007), we found an unexpected and contrasting enhancement in AP firing rate after TBF (Fig. 1*H–I*, Fig. 2*F*). This was coupled with changes in the firing patterns of neuron, whereby there

was an occurrence of doublets at the beginning of the voltage response, quantified as a significant reduction in the first ISI after TBF (Fig. 2*G*). This form of contrasting plasticity was consistently reproducible (*n*=32; Table 1) with measurements significantly different from 45 min control recordings (*n*=10) where no plasticity induction protocol was employed (Fig. 2).

In one set of experiments, we performed physiological measurements before and after TBF at the respective RMP values *without* injecting current to maintain membrane potential at the initial value of the RMP (Supplementary Fig. S1). We found consistent TBF-induced reductions in input resistance and concomitant increases in firing rate, even when measurements were made at respective RMP values (Supplementary Fig. S1). Importantly, there was significant cell-to-cell variability in the amount of plasticity expressed in each of the different measurements we employed, pointing to the expression of plasticity heterogeneities in the granule cell population. However, heterogeneities in TBF-induced sub- or supra-threshold plasticity did not show strong correlations with heterogeneities in baseline neuronal intrinsic properties (Supplementary Fig. S2). Together, our results show that TBF yielded concomitant yet contrasting plasticity of sub- and supra-threshold intrinsic excitability in DG granule cells.

TBF-induced plasticity in AP firing rate is consequent to a competition between changes in sub-threshold excitability and AP threshold.

We quantified changes in 13 different sub- and supra-threshold measurements to assess the multifarious TBF-induced changes in granule cell physiology. Pairwise scatter plots of TBF-induced concomitant changes in these measurements revealed pronounced cell-to-cell variability in the expression of plasticity in each of these measurements (Fig. 3). Are heterogeneities in TBF-induced plasticity in these measurements related to each other, whereby specific pairs of measurements exhibited correlated changes despite each measurement manifesting

heterogeneities? To assess this, we computed pairwise Pearson's correlation between the TBF-induced percentage changes in each of the 13 individual measurements (Fig. 3). Among measurements that exhibited strong positive correlations in their TBF-induced changes were between measures of sub-threshold excitability (R_{in}, $|Z|_{\max}$, S_{α}) and between AP measurements (V_{AP}, $V_{\text{AP}}^{\text{peak}}$, V_{AP}, $\left.\frac{dV}{dt}\right|_{\text{AP}}^{\max}$, $\left.\frac{dV}{dt}\right|_{\text{AP}}^{\min}$). On the other hand, TBF-induced changes in AP half width showed strong negative correlations with each of changes in V_{AP}, $V_{\text{AP}}^{\text{peak}}$, V_{AP}, $\left.\frac{dV}{dt}\right|_{\text{AP}}^{\max}$, $\left.\frac{dV}{dt}\right|_{\text{AP}}^{\min}$, and changes in latency to first spike exhibited strong negative correlations with changes in AP threshold, and AP firing. Importantly, we noted strong correlations between changes in AP firing rate and changes in AP threshold, suggesting that changes in AP threshold could be mediating the enhanced firing rate despite a reduction in subthreshold excitability. The two groups of strongly correlated changes (Group 1: subthreshold measurements; Group 2: AP measurements), in conjunction with this strong relationship between AP firing and AP threshold changes suggested that TBF-induced changes in firing rate were regulated by two concurrent yet competing mechanisms. The first is a reduction in subthreshold excitability that reduces firing rate and the second is a hyperpolarizing shift in the AP threshold that would enhance AP firing. We noted that the absence of strong correlations (positive or negative) between changes in sub- *vs*. suprathreshold measurements could be consequent to this competition. Together, the contrasting changes introduced in sub- *vs*. supra-threshold measurements, in conjunction with the competition between subthreshold excitability and AP threshold in regulating firing rate pointed to conjunctive changes in multiple ion channels that mediated TBF-induced intrinsic plasticity in DG granule cells.

Signature changes in several physiological measurements point to HCN channels as a candidate mechanism behind TBF-induced reduction in sub-threshold excitability.

There is evidence for the expression of HCN channels in granule cells and for a role of these channels in certain pathophysiological conditions (Bender et al., 2003; Krueppel et al., 2011; Stegen et al., 2012; Surges et al., 2012). Focusing on TBF-induced changes in sub-threshold measurements, in our study, we observed a depolarizing shift in the resting membrane potential and reductions in input resistance, maximal impedance amplitude and temporal summation. These changes are broadly consistent with an increased current passage through HCN channels, which are hyperpolarization-activated channels that mediate an inward current that is active under resting conditions. Specifically, it has been shown that increases in HCN channels and the associated *h* current result in depolarization of resting membrane potential, a reduction of input resistance, impedance amplitude and temporal summation (Gasparini and DiFrancesco, 1997; Magee, 1998, 1999; Hutcheon and Yarom, 2000; Narayanan and Johnston, 2007; Narayanan et al., 2010; Stegen et al., 2012; Ashhad et al., 2015).

Motivated by these observations, we asked if other TBF-induced changes in sub-threshold physiological measurements of granule cells were also consistent with changes in HCN channels. First, as HCN channels are slow conductances, their impact on neuronal excitability for relatively high-frequency inputs is low as the slow activation and deactivation profiles of these channels are inconsistent with such fast inputs. This has been employed (Narayanan and Johnston, 2008; Narayanan et al., 2010) as an effective mechanism to distinguish between changes in leak conductance (which would change excitability equally at all frequencies) or membrane capacitance (which would alter excitability preferentially at higher frequencies) or HCN channels (which would alter excitability preferentially at lower frequencies). To assess this,

we quantified changes in impedance amplitude as a function of frequency, and asked if changes were predominantly at lower frequencies (Fig. 4*A–B*). We observed significantly higher TBF-induced changes in impedance amplitude at lower frequencies compared to changes in impedance amplitude at higher frequencies (Fig. 4*A–B*), again pointing to changes in HCN channels as a substrate for TBF-induced subthreshold changes. In contrast, changes in impedance amplitude were negligible in control experiments where no activity-dependent protocol was presented (Fig. 4*A–B*). These analyses point to the ability of impedance to discern important underlying differences, owing to the frequency-dependent nature of the measurements. As neurons seldom receive steady-state inputs under ethological conditions, impedance constitutes a better measure of excitability than measures based on pulse-current injections (Narayanan and Johnston, 2008).

Our results thus far point to changes in a sub-threshold conductance that is active at rest, as all our measurements were obtained at the initial RMP. If this conductance that is active at rest were a depolarization-activated conductance, TBF-induced changes in voltage responses to depolarizing current pulses (where the channel is activated/deactivated) would be larger compared to responses to hyperpolarizing pulses (which is relatively beyond the channel's activation/deactivation range). On the other hand, a hyperpolarization-activated conductance would show an opposite response profile, whereby there would be larger changes to hyperpolarized current injections compared to depolarized current injections. If the amount of changes were invariant to hyperpolarizing and depolarizing pulses, it would point to changes in a voltage-independent conductance or in a conductance whose activation/deactivation profile is linear within the range of measurement. To assess this, we calculated TBF-induced changes in two measures of input resistance, computed independently from voltage responses to

depolarizing (R_{in}^{+}) or hyperpolarizing (R_{in}^{-}) current injections (Fig. 4*C*). We performed this analysis both for control and TBF experiments and observed no significant difference between percentage changes in R_{in}^{+} *vs.* R_{in}^{-} for either control or TBF experiments (Fig. 4*D*). However, consistent with prior observations on R_{in} (Fig. 2), the percentage changes in R_{in}^{+} or R_{in}^{-} between control and TBF experiments were highly significant (Fig. 4*D*). These observations point to TBF-induced changes in a resting conductance whose activation profile is broadly linear in the range explored here, thereby ruling out the involvement of most depolarization-activated conductances.

Together, signature TBF-induced changes in several physiological measurements (Table 1), — including depolarization in membrane potential, reductions in temporal summation (Figs. 1–2), dominant changes in excitability for inputs with lower frequencies (Fig. 4*A–B*) and consistent changes in input resistance for positive *vs.* negative pulse currents (Fig. 4*C–D*), — strongly point to a role for changes in HCN channels as the mechanism underlying the observed reduction in sub-threshold excitability.

HCN channels mediate TBF-induced reduction in sub-threshold excitability of DG granule cells.

Encouraged by the consistent and strong lines of evidence from several physiological measurements on the potential role of HCN channels in mediating TBF-induced reduction in sub-threshold excitability, we directly tested the hypothesis by performing TBF experiments in presence of ZD7288, an established HCN channel blocker. Given the several non-specificities of ZD7288 (Chevaleyre and Castillo, 2002; Chen, 2004; Sanchez-Alonso et al., 2008), especially at higher concentrations, we employed 20 μM of ZD7288 in our experiments.

First, we tested the time-dependent effect of HCN blocker on intrinsic properties of DG granule cells. In these control experiments, we found a slow yet significant increase in input resistance over a period of 45 minutes (Fig. 5*A–C*), which also reflected as increases in maximal impedance amplitude (Fig. 5*D–E*). Next, we performed TBF experiments in the presence of ZD7288, and found R_{in} and $|Z|_{max}$ to increase with time, with the strength of increases across TBF experiments statistically insignificant when compared to control experiments performed in the presence of ZD7288 (Fig. 5*A–E*, Fig. 5*G*). These results demonstrated that TBF-induced reduction in sub-threshold excitability (Fig. 2) did not express when HCN channels were blocked. Importantly, TBF-induced enhancement in supra-threshold excitability, manifesting as increased firing rate was not blocked by the presence of ZD7288 (Fig. 5*F*).

Together, our results obtained with pharmacological agents blocking HCN channels added further lines of evidence for a role of HCN channels in mediating TBF-induced reduction in sub-threshold excitability of DG granule cells. In addition, consistent with our previous analyses based on measurement correlations (Fig. 3), the dissociation in blockade of sub- *vs.* supra-threshold measurements by ZD7288 pointed to the role of another channel conductance in mediating TBF-induced supra-threshold excitability.

Riluzole, an inhibitor of persistent sodium channels, reduced firing rate of DG granule cells.

Our observations on TBF-induced enhancement in supra-threshold excitability pointed to changes in a regenerative conductance. Motivated by the expression of a persistent sodium (NaP) channel in DG granule cells predominantly in axon initial segments (Ellerkmann et al., 2003; Epsztein et al., 2010; Kress et al., 2010; Artinian et al., 2011), and the role of these channels in regulating action potential firing properties in several neuronal subtypes (Crill, 1996), we first

assessed a role for NaP channel in regulating DG granule cell excitability. We performed whole-cell current clamp recordings, measured baseline sub- and supra-threshold properties of DG granule cells, and then repeated these measurements in the presence of 20 μM riluzole (Fig. 6*A–D*), an established inhibitor of persistent sodium currents (Song et al., 1997; Urbani and Belluzzi, 2000). Even though riluzole has been widely used as a clinical drug for psychological treatments and has been tested widely for its effect on DG physiology (Kim et al., 2007; Gourley et al., 2012), its effect on physiological properties of single neurons has not been studied. When we performed before-after measurements from DG granule cells using riluzole, we found that riluzole introduced no significant changes to resting membrane potential (Fig. 6*E*), sub-threshold excitability (Fig. 6*F,* 6*I*) across different voltages (Fig. 6*G,* 6*J*) or temporal summation (Fig. 6*H*). In striking contrast, there was a pronounced reduction in firing rate of granule cells (Fig. 6*K–L*) after application of riluzole, without significant changes to AP properties (Supplementary Figure S3). These results provided further evidence for a role of persistent sodium channels in the regulation of supra-threshold excitability in DG granule cells.

Plasticity in NaP channel results in TBF-induced increase in supra-threshold excitability of DG granule cells.

We performed the long-term (45 min) control experiments in presence of riluzole without the theta burst firing protocol to examine any time dependent changes introduced by riluzole in intrinsic measurements. Although riluzole didn't alter input resistance with acute treatment (Fig. 6), we observed a significant reduction in input resistance over a 45-min period (Fig. 6*A–C*). This was observed even when we pre-treated the slice with riluzole before beginning our recordings. However, consistent with our observation under acute treatment of riluzole (Fig. 6), impedance amplitude didn't change over the course of the period in control experiments. We

now performed TBF experiments in the presence of riluzole and compared these outcomes with riluzole control experiments (Fig. 7). We confirmed that the TBF protocol elicited 150 action potentials through the protocol period (Supplementary Fig. S3*N*), and there was no difference in action potential firing pattern in the presence of riluzole. We found that TBF-induced reduction in input resistance was abolished in the presence of riluzole (Fig. 7*B–C*). In addition, analysis of $|Z|_{max}$ in riluzole experiments without and with TBF presented clear evidence for the absence of any change in subthreshold excitability after TBF in the presence of riluzole (Fig. 7*D–F*). More importantly, the firing rate changes induced by TBF (Fig. 2*F*) was completely abolished in presence of riluzole with no further increase in firing rate post-TBF (Fig. 7*G*). We found that riluzole abolished TBF-induced changes in all sub-threshold measurements (Fig 7*H*), as no significant difference was observed between control and TBF groups in the presence of riluzole. In this case, we could not quantify changes in AP properties as neurons did not fire at 250 pA for most of the recordings (both control and TBF groups).

Together, the direction of changes in several physiological measurements (Figs. 2–4), TBF experiments with ZD7288 (Fig. 5) or riluzole (Fig. 7) provided lines of evidence for conjunctive changes in HCN and persistent sodium channels in mediating the contrasting TBF-induced plasticity profiles observed in sub- *vs*. supra-threshold changes in DG granule cells.

Activity-dependent intrinsic plasticity in DG granule cells is calcium dependent.

Several forms of neuronal plasticity are dependent on the prominent second messenger calcium. The magnitude and dynamics of calcium entry into the cytosol are well-established regulators of distinct signaling cascades, with cooperation and competition across different downstream cascades yielding different directions and strengths of plasticity in disparate neural components. Therefore, we asked if TBF-induced plasticity in DG granule cells was indeed dependent on

calcium influx into the cytosol. To investigate this, we performed a set of control and TBF experiments in the presence of 30 mM BAPTA, a fast calcium chelator, in the patch pipette. We found no significant change in any measurement during control experiments in the presence of BAPTA in the pipette (Fig. 8). Importantly, when we monitored TBF-induced changes in the presence of BAPTA, we observed no significant activity-dependent change in any of the sub- or supra-threshold measurements (Fig. 8). We noticed that the overall firing rate of the cell was significantly high in presence of BAPTA in the pipette in both control as well as TBF experiments, pointing to a critical role of calcium-activated potassium channels in suppressing the excitability of DG granule cells (Aradi and Holmes, 1999; Sailer et al., 2002; Brenner et al., 2005; Mateos-Aparicio et al., 2014).

Activity-dependent intrinsic plasticity is invariant to blockade of synaptic receptors.

The plasticity induction protocol employed in this study for expression of intrinsic changes does not involve stimulation of synaptic receptors as the theta burst current pattern was injected directly into the soma. But, it is possible that different receptors driven by spontaneous activity could have interacted with intrinsic firing to play a role in plasticity induction (Fan et al., 2005). To test this, we performed TBF experiments in the presence of AMPAR, $GABA_AR$ and $GABA_BR$ antagonists (Fig. 9; Synaptic blockers). We found that the presence of synaptic blockers did not alter expression of TBF-induced plasticity (Fig. 9; Synaptic blockers), although there was quantitatively less supra-threshold plasticity especially for lower current injections (Fig. 9*F*; Synaptic blockers. *cf.* Fig. 2*F*, TBF).

What component provided calcium influx into the cytosol that was essential for plasticity induction (Fig. 8)? We hypothesized NMDAR as a potential source of calcium, whereby spontaneous activity in conjunction with action potential firing could have resulted in influx of

calcium into the cytosol (Fan et al., 2005). To test the hypothesis, we performed TBF experiments in presence of AP5, an NMDAR antagonist, and found TBF-induced sub- and supra-threshold plasticity to be independent of NMDARs (Fig. 9; AP5), although TBF-induced changes in AP firing (Fig. 9*F*; AP5. *cf.* Fig. 2*F*, TBF) and certain AP properties (Fig. 9*G*) were quantitatively higher in the presence of AP5.

Activity dependent intrinsic plasticity is mediated by calcium influx through *L*-type calcium channels and inositol trisphosphate receptors.

We hypothesized that repetitive firing triggered by the TBF protocol could recruit voltage-gated calcium channels (VGCCs) expressed in the granule cells as a source for calcium influx into the cytosol. To test this, we performed TBF experiments in presence of nimodipine and compared the results with the control recordings (with nimodipine in the bath, but without TBF). We found that TBF-induced changes in both the sub- (Fig. 10*A–E*) and supra-threshold (Fig. 10*F–G*) measurements were abolished in presence of nimodipine. Specifically, in the presence of nimodipine, TBF-induced reduction in both input resistance (Fig. 10*A–C*) and $|Z|_{max}$ (Fig. 10*D–E*) were abolished, apart from the absence of the associated increase in action potential firing rate (Fig. 10*F*).

Finally, although the extracellular fluid is a prominent source for cytosolic calcium, calcium influx into the cytosol could also be through calcium channels expressed on the membrane of the endoplasmic reticulum (ER). Motivated by the results obtained from nimodipine experiments and expression of inositol trisphosphate ($InsP_3$) receptors in DG granule cells (Fotuhi et al., 1993; Sharp et al., 1993; Hertle and Yeckel, 2007; Nicolay et al., 2007), we asked if ER calcium stores could also be a source of cytosolic calcium. We performed TBF in the presence of heparin, an established blocker of $InsP_3$ receptors. We found that TBF-induced

changes in various sub- and supra-threshold measurements were abolished in presence of heparin, providing evidence for ER calcium stores as a potential source for the induction of this form of plasticity (Fig. 11).

Together, these experiments established that synergistic interactions between *L*-type calcium channels on the plasma membrane and $InsP_3$ receptors on the ER membrane resulted in cytosolic calcium influx that mediated TBF-induced intrinsic plasticity.

DISCUSSION

In this study, we showed that the behaviorally relevant theta-burst firing protocol reliably induced long-term intrinsic plasticity in dentate gyrus granule cells. We demonstrated that this intrinsic plasticity involved contrasting changes in sub- and supra-threshold measurements, with a reduction in sub-threshold excitability accompanying an enhancement in supra-threshold excitability. We reasoned that this form of activity-dependent plasticity should recruit changes in multiple ion channels, on the basis of our analyses involving a constellation of physiological measurements that changed with TBF. Through a combination of experiments involving pharmacological and analyses of physiological changes induced by TBF, we provide strong lines of evidence for this form of plasticity to involve conjunctive changes in at least two distinct ion channels. Specifically, we showed that HCN-channel plasticity mediated TBF-induced reduction in sub-threshold excitability whereas plasticity in persistent sodium channels resulted in the accompanying increase in supra-threshold excitability. The calcium-dependence of TBF-induced intrinsic plasticity was evidenced from the blockade of plasticity by cytosolic BAPTA, a fast calcium chelator. Although TBF-induced intrinsic plasticity persisted in the presence of synaptic blockers (including NMDARs), nimodipine and cytosolic heparin independently blocked plasticity, suggesting the involvement of *L*-type calcium channels and inositol trisphosphate receptors as calcium sources.

Activity-dependent intrinsic plasticity in DG granule cells and engram cell formation.

Our study presents an important observation that DG granule cells are capable of expressing activity-dependent intrinsic plasticity *without* synaptic stimulation. We also demonstrate contrasting plasticity in sub- *vs.* supra-threshold excitability as a consequence of conjunctive changes in two distinct ion channel subtypes. The expression of cell-autonomous intrinsic

plasticity expands the available repertoire of cellular substrates for information storage, from the perspective of what all can change in response to activity patterns (Zhang and Linden, 2003; Kim and Linden, 2007; Lopez-Rojas et al., 2016; Titley et al., 2017; Rathour and Narayanan, 2019). These observations also extend to the formation of "engram cells", whereby neuron-specific enhancement in excitability could play critical roles in the emergence of cells that encode a specific context (Gallistel, 2017; Titley et al., 2017; Tonegawa et al., 2018; Pignatelli et al., 2019; Rao-Ruiz et al., 2019). We postulate that the activity-dependent increase in firing rate demonstrated in our study (Fig. 2), along with other forms of plasticity, could assist in the formation of engram cells.

Furthermore, the manifestation of cell-to-cell variability (Fig. 2–3) in activity-dependent intrinsic plasticity could form a cellular substrate for why certain neurons (and not others) are primed to become engram cells (Yiu et al., 2014; Josselyn and Frankland, 2018; Pignatelli et al., 2019; Rao-Ruiz et al., 2019). Specifically, across measurements, whereas certain neurons showed tremendous changes in response to the same activity pattern, others did not (Figs. 2–4). Additionally, expression of enhancement of supra-threshold excitability as a consequence of TBF was reliant on a *competition* between two opposing changes (in sub-threshold excitability and in AP threshold). Together, the sparse and orthogonal connectivity patterns in the DG, in conjunction with such competition among plasticity in different components could play a critical role in regulating resource allocation for memory storage (Li et al., 2017; Josselyn and Frankland, 2018; Lodge and Bischofberger, 2019; Rao-Ruiz et al., 2019).

Conjunctive plasticity in multiple ion channels points to plasticity manifolds.

We demonstrated that the *same* plasticity protocol induces conjunctive plasticity in different channels. We argue that such conjunctive plasticity points to the presence of a tightly regulated

plasticity manifold, whereby changes to different cellular components are not arbitrary but follow specific rules enforced by common or coupled molecular signaling cascades regulating such plasticity. The plasticity manifold is reminiscent of neuronal intrinsic manifold and behavioral manifold defined in the context of natural *vs.* unnatural neuronal activity and behavior (Jazayeri and Afraz, 2017; Krakauer et al., 2017). Akin to tightly interconnected patterns of activity across neurons, plasticity in neural components, despite being ubiquitous, seems to follow specific rules on how different components *covary* (Kim and Linden, 2007; Nelson and Turrigiano, 2008; O'Leary et al., 2013; O'Leary et al., 2014; Srikanth and Narayanan, 2015; Rathour and Narayanan, 2019). These rules are enforced by signaling cascades that target specific sets of downstream components, in a manner that seems to also depend on the specific patterns of afferent inputs and the input state of the neuron (Rathour and Narayanan, 2019). Our results show a further instance of the manifestation of such plasticity manifold whereby two distinct channels change concomitantly, introducing conjunctive changes resulting in competition among them to define supra-threshold excitability.

There are advantages of tightly regulated plasticity manifolds involving conjunctive plasticity in different structural components. For instance, our study presents a possible intrinsic route that a neuron could pursue to concomitantly achieve homeostasis while encoding or storage of information. Specifically, from the perspective of engram formation, we had earlier postulated that the activity-dependent increase in firing rate could assist the formation of engram cells that encode for a given context. Within such a postulate, the concomitant reduction in sub-threshold excitability would ensure that the response of the cell to other behavioral contexts is suppressed, apart from maintaining homeostatic balance (to compensate for the enhanced firing rate of the cell). Thus, the *contrasting* patterns of plasticity in sub- *vs.* supra-threshold excitability could be

a cell-autonomous substrate to encode new information through enhanced excitability, accompanied by a mechanism to enhance specificity to specific contexts and to enable homeostatic balance of overall afferent drive to the neuron (Nelson and Turrigiano, 2008; Turrigiano, 2011). This is reminiscent of plasticity manifolds in CA1 pyramidal neurons, whereby the *same* theta-burst pairing protocol induces putative *mnemonic* changes in synaptic strength (Magee and Johnston, 1997), in transient potassium channels (Frick et al., 2004; Losonczy et al., 2008), and in SK channels (Lin et al., 2008), apart from concomitantly inducing putative *homeostatic* changes in HCN channels (Fan et al., 2005; Narayanan and Johnston, 2007, 2010; Honnuraiah and Narayanan, 2013). In our study, we show that the *mnemonic* role could be played by plasticity in persistent sodium channels and the *homeostatic* part could be played by changes in HCN channels. Thus, conjunctive plasticity involving multiple neural components forms an ideal substrate for effectively achieving the twin goal of encoding and homeostasis (Rathour and Narayanan, 2019) in a cell-type dependent manner, with plasticity manifolds acting as a mechanistic basis for population activity to remain within the neuronal activity manifold.

Implications for activity-dependent intrinsic plasticity to metaplasticity and channelopathies.

It is now well established that plasticity in intrinsic properties could result in metaplasticity through changes in excitability and in temporal summation (Narayanan and Johnston, 2010; Hulme et al., 2013; Sehgal et al., 2013; Anirudhan and Narayanan, 2015). Our results, demonstrating changes to temporal summation and to sub- and supra-threshold excitability would therefore result in metaplasticity in synaptic plasticity profiles of the dentate gyrus. Such metaplasticity introduced intrinsic plasticity could also form a putative substrate for changes in threshold for synaptic plasticity by *prior* theta-frequency synaptic activity (Christie et al., 1995;

Abraham, 2008). Specifically, prior theta-frequency synaptic activity could have induced changes in intrinsic properties, which in turn could have altered the synaptic plasticity profiles resulting in altered thresholds observed under certain experimental conditions.

From the pathophysiological perspective, altered activity patterns have been associated with intrinsic plasticity in the dentate gyrus, including in channels explored in this study (Bender et al., 2003; Beck and Yaari, 2008; Stegen et al., 2009; Young et al., 2009; Stegen et al., 2012; Surges et al., 2012; Yim et al., 2015). Intrinsic plasticity mechanisms that are explored in this study could play a role in the presence of pathological activity patterns as well. These channelopathies could be homeostatic or could exacerbate the pathological activity patterns in a manner that is known to be dependent on several internal and external factors (Johnston et al., 2000b; Johnston et al., 2000a; Kullmann, 2002; Beck and Yaari, 2008; Kullmann and Waxman, 2010; Terzic and Perez-Terzic, 2010; Lerche et al., 2012; Poolos and Johnston, 2012; Brager and Johnston, 2014; Johnston et al., 2016).

Limitations, caveats and future directions.

Although we do not know the specific reasons for a time-dependent reduction in input resistance in the presence of riluzole (Fig. 7), it could be a consequence of the action of riluzole on one of its several known targets (Bryson et al., 1996; Doble, 1996; Duprat et al., 2000; Frizzo et al., 2004; Fumagalli et al., 2008; Dimitriadi et al., 2013). Among these is the ability of riluzole to activate two pore domain potassium channels, targeting specific subunits (Duprat et al., 2000) that are known to express and alter excitability of DG granule cells (Reyes et al., 2000; Yarishkin et al., 2014). Such activation of two-pore domain potassium channels could potentially explain the time dependent reduction in input resistance we observed.

With reference to the mechanistic basis of TBF-induced plasticity, future studies should more thoroughly explore the different calcium sources participating in the induction of this plasticity. Our study unveils a role for ER calcium in this form of plasticity, and suggests AP-induced influx of calcium through *L*-type calcium channels as a source for initiating such release through $InsP_3$ receptors. In addition to these, future studies should explore the possibility of $InsP_3$ receptor activation through the recruitment of metabotropic receptors and the role of the initial rise of cytosolic calcium (through VGCCs) in activating ryanodine receptors, resulting in calcium release from the stores (Bezprozvanny et al., 1991; Sharp et al., 1993; O'Mara et al., 1995; Wang et al., 1996; Berridge et al., 2000; Rose and Konnerth, 2001; Choe and Ehrlich, 2006; Hertle and Yeckel, 2007; Lanner et al., 2010; Ross, 2012). The role of different metabotropic receptors, ryanodine receptor and other voltage-gated calcium channels in mediating TBF-induced plasticity needs further exploration. Importantly, future studies should explore the specific signaling cascades, downstream of calcium influx, that mediate the conjunctive plasticity in these ion channels.

Although our focus in this study was on the somata of DG granule cells and on two specific ion channels, it is possible that other channels might change in response to TBF and the manifestation of plasticity might be distinct at different somato-dendritic locations. Therefore, future studies should assess plasticity in other channels employing whole-cell current clamp recordings, voltage imaging, calcium imaging and cell-attached recordings for locations spanning the somato-dendritic axis of DG granule cells, and explore the roles of other channels employing pharmacological analysis during such recordings. This is important because the localization profile of plasticity is important in assessing their implications to specific functions, and such analyses would provide the complete span of the plasticity manifold with reference to

this form of intrinsic plasticity (Frick et al., 2004; Narayanan and Johnston, 2007; Lin et al., 2008; Narayanan and Johnston, 2008; Narayanan et al., 2010; Narayanan and Johnston, 2012; Adam et al., 2019).

Apart from spanning the somatodendritic axis of granule cells, future studies should also explore TBF-induced intrinsic plasticity across the dorso-ventral, superficial-deep and infrapyramidal-suprapyramidal axes of the dentate gyrus (Amaral et al., 2007) to assess potential differences in plasticity expression across different subregions of the dentate gyrus. In this context, although there are several studies exploring differences in synaptic plasticity profiles in mature *vs.* immature neurons of the DG (Schmidt-Hieber et al., 2004; Aimone et al., 2011; Dieni et al., 2013; Aimone et al., 2014; Kropff et al., 2015; Li et al., 2017), potential differences in intrinsic plasticity profiles between mature *vs.* immature neurons has not been thoroughly explored. These differences might play a role in how immature neurons integrate into a functional network, and how they participate in engram formation with reference to a specific context. Along the same lines, although the role of different neuromodulators on synaptic plasticity has been explored more thoroughly, the impact of neuromodulatory inputs on intrinsic plasticity profiles has not been explored. Future studies should explore the role of adult neurogenesis and neuromodulators in induction and expression of intrinsic plasticity.

MATERIALS AND METHODS

Ethical approval

All experiments reported in this study were performed in strict adherence to the protocols cleared by the Institute Animal Ethics Committee (IAEC) of the Indian Institute of Science, Bangalore. Animals were provided *ad libitum* food and water and were housed with an automated 12 h light–12h dark cycle. All animals were obtained from the in-house breeding setup at the central animal facility of the Indian Institute of Science. Surgical and electrophysiological procedures were similar to previously established protocols (Narayanan and Johnston, 2007, 2008; Narayanan et al., 2010; Ashhad et al., 2015; Ashhad and Narayanan, 2016; Rathour et al., 2016; Das and Narayanan, 2017) and are detailed below.

Slice preparation for *in-vitro* patch clamp recording

Male Sprague-Dawley rats of 5- to 8-weeks age were anesthetized by intraperitoneal injection of a ketamine-xylazine mixture. After onset of deep anesthesia, assessed by cessation of toe-pinch reflex, transcardial perfusion of ice-cold cutting solution was performed. The cutting solution contained 2.5 mM KCl, 1.25 mM NaH_2PO_4, 25 mM $NaHCO_3$, 0.5 mM $CaCl_2$, 7 mM $MgCl_2$, 7 mM dextrose, 3 mM sodium pyruvate, and 200 mM sucrose (pH 7.3, ~300 mOsm) saturated with 95% O_2 and 5% CO_2. Thereafter, the brain was removed quickly and 350-µm thick near-horizontal slices were prepared from middle hippocampi (Bregma, –6.5 mm to –5.1 mm), using a vibrating blade microtome (Leica Vibratome), while submerged in ice-cold cutting solution saturated with 95% O_2 and 5% CO_2. The slices were then incubated for 10–15 mins at 34° C in a chamber containing the holding solution (pH 7.3, ~300 mOsm) with the composition of: 125 mM NaCl, 2.5 mM KCl, 1.25 mM NaH_2PO_4, 25 mM $NaHCO_3$, 2 mM $CaCl_2$, 2 mM $MgCl_2$, 10 mM

dextrose, 3 mM sodium pyruvate saturated with 95% O_2 and 5% CO_2. The slices were kept in a holding chamber at room temperature for at least 45 min before the start of recordings.

Electrophysiology: Whole-cell current-clamp recording

For electrophysiological recordings, slices were transferred to the recording chamber and continuously perfused with carbogenated artificial cerebrospinal fluid (ACSF/extracellular recording solution) at a flow rate of 2–3 mL/min. All neuronal recordings were performed under current-clamp configuration at physiological temperatures (32–35° C), achieved through an inline heater that was part of a closed-loop temperature control system (Harvard Apparatus). The carbogenated ACSF contained 125 mM NaCl, 3 mM KCl, 1.25 mM NaH_2PO_4, 25 mM $NaHCO_3$, 2 mM $CaCl_2$, 1 mM $MgCl_2$, 10 mM dextrose (pH 7.3; ~300 mOsm). Slices were first visualized under a 10× objective lens to locate the granule cell layer in the crest sector of the dentate gyrus (Amaral et al., 2007). Then, a 63× water immersion objective lens was employed to perform patch-clamp recordings from DG granule cells in the crest sector, through a Dodt contrast microscope (Carl Zeiss Axioexaminer). Whole-cell current-clamp recordings were performed from visually identified dentate gyrus granule cell somata, using Dagan BVC-700A amplifiers. Images of cell location were captured for record and for post-facto confirmation of the region where the cell belonged. Borosilicate glass electrodes with resistance between 2–6 MΩ (more often electrodes with ~4 MΩ electrode resistance were used) were pulled (P-97 Flaming/Brown micropipette puller; Sutter) from thick glass capillaries (1.5 mm outer diameter and 0.86 mm inner diameter; Sutter) and used for patch-clamp recordings. The pipette solution contained 120 mM K-gluconate, 20 mM KCl, 10 mM HEPES, 4 mM NaCl, 4 mM Mg-ATP, 0.3 mM Na-GTP, and 7 mM K2-phosphocreatine (pH 7.3 adjusted with KOH, osmolarity ~300 mOsm).

Series resistance was monitored and compensated online using the bridge-balance circuit of the amplifier. Experiments were discarded only if the initial resting membrane potential was more depolarized than –60 mV or if series resistance rose above 30 MΩ, or if there were fluctuations in temperature and ACSF flow rate during the course of the experiment. Unless otherwise stated, experiments were performed at the initial resting membrane potential (reported here as V_{RMP}) of the cell. Voltages have not been corrected for the liquid junction potential, which was experimentally measured to be ~8 mV.

Sub-threshold measurements

We characterized plasticity in intrinsic properties of DG granule neurons using several electrophysiological measurements obtained through several pulse-current and frequency-dependent current injections (Narayanan and Johnston, 2007, 2008; Narayanan et al., 2010; Ashhad et al., 2015; Ashhad and Narayanan, 2016; Malik et al., 2016; Rathour et al., 2016; Das and Narayanan, 2017; Mishra and Narayanan, 2019). Input resistance (R_{in}) was measured as the slope of a linear fit to the steady-state *V-I* plot obtained by injecting subthreshold current pulses of amplitudes spanning –25 to +25 pA, in steps of 5 pA (Fig. 1*D*). To assess temporal summation, five α-excitatory postsynaptic potentials (α-EPSPs) with 50 ms interval were evoked by current injections of the form $I_\alpha = I_{max}\, t \exp(-\alpha t)$, with $\alpha = 0.1$ ms^{-1} (Fig. 1*G*). Temporal summation ratio (S_α) in this train of five EPSPs was computed as E_{last}/E_{first}, where E_{last} and E_{first} were the amplitudes of last and first EPSPs in the train, respectively. Percentage sag was measured from the voltage response of the cell to a hyperpolarizing current pulse of 100 pA and was defined as 100 $(1-V_{ss}/V_{peak})$, where V_{ss} and V_{peak} depicted the steady-state and peak voltage deflection from V_{RMP}, respectively.

The chirp stimulus (Fig. 1*B*) used for characterizing the impedance amplitude (ZAP) profiles was a sinusoidal current of constant amplitude below firing threshold, with its frequency linearly spanning 0–15 Hz in 15 s (*Chirp15*). The magnitude of the ratio of the Fourier transform of the voltage response (Fig. 1*E*) to the Fourier transform of the *Chirp15* stimulus formed the ZAP (Fig. 1*F*):

$$|Z(f)| = \sqrt{(\mathrm{Re}(Z(f))^2 + (\mathrm{Im}(Z(f))^2}$$

where Re($Z(f)$) and Im($Z(f)$) refer to the real and imaginary parts of the impedance Z as a function of frequency f. The maximum value of impedance across all frequencies was measured as the maximum impedance amplitude ($|Z|_{\max}$; Fig. 1*F*). The frequency at which the impedance amplitude reached its maximum was the resonance frequency (f_R). Resonance strength (Q) was measured as the ratio of the maximum impedance amplitude to the impedance amplitude at 0.5 Hz (Hu et al., 2002; Narayanan and Johnston, 2007).

Supra-threshold measurements

To understand the possible cellular mechanisms underlying the expression of activity-dependent intrinsic plasticity, we further analyzed the various features of action potentials (AP). First, AP firing frequency was computed by extrapolating the number of spikes obtained during a 700 ms current injection to 1 s. Current amplitude of these pulse-current injections was varied from 0 pA to 250 pA in steps of 50 pA, to construct the firing frequency *vs.* injected current (*f–I*) plot (Fig. 1*H–I*). Various AP related measurements (Malik et al., 2016; Mishra and Narayanan, 2019) were derived from the voltage response of the cell to a 250 pA pulse-current injection. AP amplitude (V_{AP}) was computed as the difference between the peak voltage of the spike (V_{AP}^{peak}) and V_{RMP}. The temporal distance between the timing of the first spike and the time of current injection was defined as latency to first spike (T_{1AP}). The duration between the first and the second spikes was

defined as the first inter-spike interval (T_{1ISI}). AP half-width (T_{APHW}) was the temporal width measured at the half-maximal points of the AP peak with reference to V_{RMP}. The maximum $\left.\frac{dV}{dt}\right|_{AP}^{max}$, and minimum $\left.\frac{dV}{dt}\right|_{AP}^{min}$ values of the AP temporal derivative were calculated from the temporal derivative of the AP trace. The voltage in the AP trace corresponding to the time point at which the dV/dt crossed 20 V/s defined AP threshold. All supra-threshold measurements were obtained through current injections into the cell resting at V_{RMP}.

Theta Burst Firing Protocol

Experimental procedures for inducing theta-burst firing (TBF) were similar to previously established protocols (Fan et al., 2005; Narayanan and Johnston, 2007). To induce TBF, we employed 3 trains of 10 theta-modulated bursts each, separated by 10 s. Each train (Fig. 1*C*) was made of a burst of 5 APs with an intra-burst frequency of 100 Hz (10 ms ISI), and the inter-burst frequency set at 5 Hz (200 ms). Each AP within the burst was initiated by injecting a large current (2 nA) of small duration (2 ms) into the neuron. The experimental protocol (Fig. 1*B*–*C*) for TBF involved initial measurements of the *V-I* curve, *f-I* curve and S_α, followed by establishment of a 5 min stable baseline while monitoring resting membrane potential and R_{in}. Monitoring of these measurements were from cell responses to the *Chirp15* stimulus, measured twice every minute, during this initial 5 min period and for 40 min after TBF, followed by a final measurement of the *V-I* curve, *f-I* curve and S_α. We recorded from one selected cell in any given slice, as the induction protocol could have had unknown effects on neighboring cells through synaptic transmission or other signaling cascades.

To assess pairwise relationship across 13 different sub- and supra-threshold measurements, we analyzed the scatter plot matrices of post-TBF changes in these measurements

(Fig. 3*A*). We computed Pearson's correlation coefficients for each of these pair-wise scatter plots and analyzed the distribution of correlation coefficients (Fig. 3).

Pharmacological Blockers

Synaptic receptor blockers: Drugs and their concentrations used in the experiments were 10 μM 6-cyano- 7-nitroquinoxaline-2,3-dione (CNQX), an AMPA receptor blocker; 10 μM (+) bicuculline and 10 μM picrotoxin, both $GABA_A$ receptor blockers; 50 μM D,L-2-amino-5-phosphonovaleric acid (D,L-APV), NMDA receptor and 2 μM CGP55845, $GABA_B$ blocker (all synaptic blockers from Allied Scientific) in the bath solution. To block *Inositol trisphosphate ($InsP_3$) receptors*, 1 mg/mL heparin (20,000 –25,000 molecular weight; Calbiochem) was included in the recording pipette.

Voltage-gated ion channel blockers: 20 μM ZD7288 (Allied Scientific), 20 μM Riluzole (Allied Scientific) and 10 μM Nimodipine (Tocris Biosciences) were used to block HCN, persistent sodium and *L*-type calcium channels, respectively. For experiments with ZD7288, cells were patched with pipette solution containing 20 μM ZD7288 along with adding it to bath solution (Rosenkranz and Johnston, 2006; Narayanan et al., 2010; Ashhad and Narayanan, 2016). For the experiments with riluzole, slices were pretreated with Riluzole for at least 15 min before the start of recordings.

Fast calcium chelator: 30 mM (1,2-bis(o-aminophenoxy)ethane-N,N,N′,N′-tetraacetic acid), BAPTA (Thermo Fisher) was incorporated into the pipette solution. The constituents of the pipette solution were (in mM): 30 mM K_4-BAPTA, 20 mM KCl, 10 mM HEPES, 4 mM NaCl, 4 mM Mg-ATP, 0.3 mM Na-GTP, and 7 mM K2-phosphocreatine (pH 7.3 adjusted with KOH, osmolarity ~300 mOsm adjusted with sucrose).

Data acquisition, analyses and representation

All data acquisition and analyses were performed using custom-written software in Igor Pro (Wavemetrics), and statistical analyses were performed using the R computing package (http://www.r-project.org/). In order to avoid false interpretations, the entire range of measurements are reported in figures rather than providing only the summary statistics (Marder and Taylor, 2011; Rathour and Narayanan, 2019). Necessary care was taken and appropriate controls were performed for each of the drugs used to ensure that there were no time-dependent changes initiated by just the presence of the drug in the bath or in the pipette solution. For all cases, we performed the controls (no protocol) and TBF experiments in the presence of same quantity of drugs, and report the entire span of measurements corresponding to the outcomes for both sets of experiments.

REFERENCES

Abraham WC (2008) Metaplasticity: tuning synapses and networks for plasticity. Nature reviews Neuroscience 9:387.

Adam Y et al. (2019) Voltage imaging and optogenetics reveal behaviour-dependent changes in hippocampal dynamics. Nature 569:413-417.

Aimone JB, Deng W, Gage FH (2011) Resolving new memories: a critical look at the dentate gyrus, adult neurogenesis, and pattern separation. Neuron 70:589-596.

Aimone JB, Li Y, Lee SW, Clemenson GD, Deng W, Gage FH (2014) Regulation and function of adult neurogenesis: from genes to cognition. Physiol Rev 94:991-1026.

Amaral DG, Scharfman HE, Lavenex P (2007) The dentate gyrus: fundamental neuroanatomical organization (dentate gyrus for dummies). Prog Brain Res 163:3-22.

Anirudhan A, Narayanan R (2015) Analogous synaptic plasticity profiles emerge from disparate channel combinations. J Neurosci 35:4691-4705.

Aradi I, Holmes WR (1999) Role of multiple calcium and calcium-dependent conductances in regulation of hippocampal dentate granule cell excitability. J Comput Neurosci 6:215-235.

Artinian J, Peret A, Marti G, Epsztein J, Crepel V (2011) Synaptic kainate receptors in interplay with INaP shift the sparse firing of dentate granule cells to a sustained rhythmic mode in temporal lobe epilepsy. J Neurosci 31:10811-10818.

Ashhad S, Narayanan R (2016) Active dendrites regulate the impact of gliotransmission on rat hippocampal pyramidal neurons. Proc Natl Acad Sci U S A 113:E3280-3289.

Ashhad S, Johnston D, Narayanan R (2015) Activation of InsP3 receptors is sufficient for inducing graded intrinsic plasticity in rat hippocampal pyramidal neurons. Journal of neurophysiology 113:2002-2013.

Bakker A, Kirwan CB, Miller M, Stark CE (2008) Pattern separation in the human hippocampal CA3 and dentate gyrus. Science 319:1640-1642.

Beck H, Yaari Y (2008) Plasticity of intrinsic neuronal properties in CNS disorders. Nature reviews Neuroscience 9:357-369.

Beck H, Goussakov IV, Lie A, Helmstaedter C, Elger CE (2000) Synaptic plasticity in the human dentate gyrus. J Neurosci 20:7080-7086.

Bender RA, Soleymani SV, Brewster AL, Nguyen ST, Beck H, Mathern GW, Baram TZ (2003) Enhanced expression of a specific hyperpolarization-activated cyclic nucleotide-gated cation channel (HCN) in surviving dentate gyrus granule cells of human and experimental epileptic hippocampus. J Neurosci 23:6826-6836.

Berridge MJ, Lipp P, Bootman MD (2000) The versatility and universality of calcium signalling. Nat Rev Mol Cell Biol 1:11-21.

Bezprozvanny I, Watras J, Ehrlich BE (1991) Bell-shaped calcium-response curves of Ins(1,4,5)P3- and calcium-gated channels from endoplasmic reticulum of cerebellum. Nature 351:751-754.

Bland BH (1986) The physiology and pharmacology of hippocampal formation theta rhythms. Progress in neurobiology 26:1-54.

Bliss TV, Lomo T (1973) Long-lasting potentiation of synaptic transmission in the dentate area of the anaesthetized rabbit following stimulation of the perforant path. J Physiol 232:331-356.

Brager DH, Johnston D (2014) Channelopathies and dendritic dysfunction in fragile X syndrome. Brain Res Bull 103C:11-17.
Brager DH, Akhavan AR, Johnston D (2012) Impaired dendritic expression and plasticity of h-channels in the fmr1(-/y) mouse model of fragile X syndrome. Cell reports 1:225-233.
Brenner R, Chen QH, Vilaythong A, Toney GM, Noebels JL, Aldrich RW (2005) BK channel beta4 subunit reduces dentate gyrus excitability and protects against temporal lobe seizures. Nat Neurosci 8:1752-1759.
Bryson HM, Fulton B, Benfield P (1996) Riluzole. A review of its pharmacodynamic and pharmacokinetic properties and therapeutic potential in amyotrophic lateral sclerosis. Drugs 52:549-563.
Buzsaki G (2002) Theta oscillations in the hippocampus. Neuron 33:325-340.
Chen C (2004) ZD7288 inhibits postsynaptic glutamate receptor-mediated responses at hippocampal perforant path-granule cell synapses. The European journal of neuroscience 19:643-649.
Chevaleyre V, Castillo PE (2002) Assessing the role of Ih channels in synaptic transmission and mossy fiber LTP. Proc Natl Acad Sci U S A 99:9538-9543.
Choe CU, Ehrlich BE (2006) The inositol 1,4,5-trisphosphate receptor (IP3R) and its regulators: sometimes good and sometimes bad teamwork. Science's STKE : signal transduction knowledge environment 2006:re15.
Christie BR, Stellwagen D, Abraham WC (1995) Reduction of the threshold for long-term potentiation by prior theta-frequency synaptic activity. Hippocampus 5:52-59.
Clemens AM, Johnston D (2014) Age- and location-dependent differences in store depletion-induced h-channel plasticity in hippocampal pyramidal neurons. Journal of neurophysiology 111:1369-1382.
Colgin LL (2013) Mechanisms and Functions of Theta Rhythms. Annual Review of Neuroscience, Vol 36 36:295-312.
Colgin LL (2016) Rhythms of the hippocampal network. Nature reviews Neuroscience 17:239-249.
Crill WE (1996) Persistent sodium current in mammalian central neurons. Annual review of physiology 58:349-362.
Danielson NB, Turi GF, Ladow M, Chavlis S, Petrantonakis PC, Poirazi P, Losonczy A (2017) In Vivo Imaging of Dentate Gyrus Mossy Cells in Behaving Mice. Neuron 93:552-559 e554.
Das A, Narayanan R (2017) Theta-frequency selectivity in the somatic spike triggered average of rat hippocampal pyramidal neurons is dependent on HCN channels. Journal of neurophysiology 118:2251-2266.
Davis CD, Jones FL, Derrick BE (2004) Novel environments enhance the induction and maintenance of long-term potentiation in the dentate gyrus. J Neurosci 24:6497-6506.
Diamantaki M, Frey M, Berens P, Preston-Ferrer P, Burgalossi A (2016) Sparse activity of identified dentate granule cells during spatial exploration. eLife 5.
Dieni CV, Nietz AK, Panichi R, Wadiche JI, Overstreet-Wadiche L (2013) Distinct determinants of sparse activation during granule cell maturation. J Neurosci 33:19131-19142.
Dimitriadi M, Kye MJ, Kalloo G, Yersak JM, Sahin M, Hart AC (2013) The neuroprotective drug riluzole acts via small conductance Ca2+-activated K+ channels to ameliorate defects in spinal muscular atrophy models. J Neurosci 33:6557-6562.

Doble A (1996) The pharmacology and mechanism of action of riluzole. Neurology 47:S233-241.
Duprat F, Lesage F, Patel AJ, Fink M, Romey G, Lazdunski M (2000) The neuroprotective agent riluzole activates the two P domain K(+) channels TREK-1 and TRAAK. Molecular pharmacology 57:906-912.
Ellerkmann RK, Remy S, Chen J, Sochivko D, Elger CE, Urban BW, Becker A, Beck H (2003) Molecular and functional changes in voltage-dependent Na(+) channels following pilocarpine-induced status epilepticus in rat dentate granule cells. Neuroscience 119:323-333.
Epsztein J, Sola E, Represa A, Ben-Ari Y, Crepel V (2010) A selective interplay between aberrant EPSPKA and INaP reduces spike timing precision in dentate granule cells of epileptic rats. Cerebral cortex 20:898-911.
Fan Y, Fricker D, Brager DH, Chen X, Lu HC, Chitwood RA, Johnston D (2005) Activity-dependent decrease of excitability in rat hippocampal neurons through increases in I(h). Nat Neurosci 8:1542-1551.
Fotuhi M, Sharp AH, Glatt CE, Hwang PM, von Krosigk M, Snyder SH, Dawson TM (1993) Differential localization of phosphoinositide-linked metabotropic glutamate receptor (mGluR1) and the inositol 1,4,5-trisphosphate receptor in rat brain. J Neurosci 13:2001-2012.
Frick A, Magee J, Johnston D (2004) LTP is accompanied by an enhanced local excitability of pyramidal neuron dendrites. Nat Neurosci 7:126-135.
Frizzo ME, Dall'Onder LP, Dalcin KB, Souza DO (2004) Riluzole enhances glutamate uptake in rat astrocyte cultures. Cell Mol Neurobiol 24:123-128.
Fumagalli E, Funicello M, Rauen T, Gobbi M, Mennini T (2008) Riluzole enhances the activity of glutamate transporters GLAST, GLT1 and EAAC1. European journal of pharmacology 578:171-176.
Gallistel CR (2017) The Coding Question. Trends Cogn Sci 21:498-508.
Gasparini S, DiFrancesco D (1997) Action of the hyperpolarization-activated current (Ih) blocker ZD 7288 in hippocampal CA1 neurons. Pflugers Archiv : European journal of physiology 435:99-106.
GoodSmith D, Chen X, Wang C, Kim SH, Song H, Burgalossi A, Christian KM, Knierim JJ (2017) Spatial Representations of Granule Cells and Mossy Cells of the Dentate Gyrus. Neuron 93:677-690 e675.
Gourley SL, Espitia JW, Sanacora G, Taylor JR (2012) Antidepressant-like properties of oral riluzole and utility of incentive disengagement models of depression in mice. Psychopharmacology 219:805-814.
Govindarajan A, Kelleher RJ, Tonegawa S (2006) A clustered plasticity model of long-term memory engrams. Nature reviews Neuroscience 7:575-583.
Greenstein YJ, Pavlides C, Winson J (1988) Long-term potentiation in the dentate gyrus is preferentially induced at theta rhythm periodicity. Brain Res 438:331-334.
Heigele S, Sultan S, Toni N, Bischofberger J (2016) Bidirectional GABAergic control of action potential firing in newborn hippocampal granule cells. Nat Neurosci 19:263-270.
Hertle DN, Yeckel MF (2007) Distribution of inositol-1,4,5-trisphosphate receptor isotypes and ryanodine receptor isotypes during maturation of the rat hippocampus. Neuroscience 150:625-638.

Honnuraiah S, Narayanan R (2013) A calcium-dependent plasticity rule for HCN channels maintains activity homeostasis and stable synaptic learning. PloS one 8:e55590.
Hu H, Vervaeke K, Storm JF (2002) Two forms of electrical resonance at theta frequencies, generated by M-current, h-current and persistent Na+ current in rat hippocampal pyramidal cells. J Physiol 545:783-805.
Hulme SR, Jones OD, Abraham WC (2013) Emerging roles of metaplasticity in behaviour and disease. Trends Neurosci 36:353-362.
Hutcheon B, Yarom Y (2000) Resonance, oscillation and the intrinsic frequency preferences of neurons. Trends Neurosci 23:216-222.
Jazayeri M, Afraz A (2017) Navigating the Neural Space in Search of the Neural Code. Neuron 93:1003-1014.
Johnston D, Narayanan R (2008) Active dendrites: colorful wings of the mysterious butterflies. Trends Neurosci 31:309-316.
Johnston D, Hoffman DA, Poolos NP (2000a) Potassium channels and dendritic function in hippocampal pyramidal neurons. Epilepsia 41:1072-1073.
Johnston D, Frick A, Poolos N (2016) Dendrites and disease. In: Dendrites, 3 Edition (Stuart G, Spruston N, Hausser M, eds). New York, NY: Oxford University Press.
Johnston D, Hoffman DA, Magee JC, Poolos NP, Watanabe S, Colbert CM, Migliore M (2000b) Dendritic potassium channels in hippocampal pyramidal neurons. J Physiol 525 Pt 1:75-81.
Josselyn SA, Frankland PW (2018) Memory Allocation: Mechanisms and Function. Annu Rev Neurosci 41:389-413.
Kim JE, Kim DS, Kwak SE, Choi HC, Song HK, Choi SY, Kwon OS, Kim YI, Kang TC (2007) Anti-glutamatergic effect of riluzole: comparison with valproic acid. Neuroscience 147:136-145.
Kim SJ, Linden DJ (2007) Ubiquitous plasticity and memory storage. Neuron 56:582-592.
Krakauer JW, Ghazanfar AA, Gomez-Marin A, MacIver MA, Poeppel D (2017) Neuroscience Needs Behavior: Correcting a Reductionist Bias. Neuron 93:480-490.
Kress GJ, Dowling MJ, Eisenman LN, Mennerick S (2010) Axonal sodium channel distribution shapes the depolarized action potential threshold of dentate granule neurons. Hippocampus 20:558-571.
Kropff E, Yang SM, Schinder AF (2015) Dynamic role of adult-born dentate granule cells in memory processing. Current opinion in neurobiology 35:21-26.
Krueppel R, Remy S, Beck H (2011) Dendritic integration in hippocampal dentate granule cells. Neuron 71:512-528.
Kullmann DM (2002) The neuronal channelopathies. Brain : a journal of neurology 125:1177-1195.
Kullmann DM, Waxman SG (2010) Neurological channelopathies: new insights into disease mechanisms and ion channel function. J Physiol 588:1823-1827.
Lanner JT, Georgiou DK, Joshi AD, Hamilton SL (2010) Ryanodine receptors: structure, expression, molecular details, and function in calcium release. Cold Spring Harb Perspect Biol 2:a003996.
Larson J, Munkacsy E (2015) Theta-burst LTP. Brain Res 1621:38-50.
Lerche H, Shah M, Beck H, Noebels JL, Johnston D, Vincent A (2012) Ion channels in genetic and acquired forms of epilepsy. J Physiol.

Leutgeb JK, Leutgeb S, Moser MB, Moser EI (2007) Pattern separation in the dentate gyrus and CA3 of the hippocampus. Science 315:961-966.
Li L, Sultan S, Heigele S, Schmidt-Salzmann C, Toni N, Bischofberger J (2017) Silent synapses generate sparse and orthogonal action potential firing in adult-born hippocampal granule cells. eLife 6.
Lin MT, Lujan R, Watanabe M, Adelman JP, Maylie J (2008) SK2 channel plasticity contributes to LTP at Schaffer collateral-CA1 synapses. Nat Neurosci 11:170-177.
Lisman J, Cooper K, Sehgal M, Silva AJ (2018) Memory formation depends on both synapse-specific modifications of synaptic strength and cell-specific increases in excitability. Nat Neurosci 21:309-314.
Lodge M, Bischofberger J (2019) Synaptic properties of newly generated granule cells support sparse coding in the adult hippocampus. Behav Brain Res 372:112036.
Lopez-Rojas J, Heine M, Kreutz MR (2016) Plasticity of intrinsic excitability in mature granule cells of the dentate gyrus. Scientific reports 6:21615.
Losonczy A, Makara JK, Magee JC (2008) Compartmentalized dendritic plasticity and input feature storage in neurons. Nature 452:436-441.
Magee JC (1998) Dendritic hyperpolarization-activated currents modify the integrative properties of hippocampal CA1 pyramidal neurons. J Neurosci 18:7613-7624.
Magee JC (1999) Dendritic lh normalizes temporal summation in hippocampal CA1 neurons. Nat Neurosci 2:508-514.
Magee JC, Johnston D (1997) A synaptically controlled, associative signal for Hebbian plasticity in hippocampal neurons. Science 275:209-213.
Malik R, Johnston D (2017) Dendritic GIRK Channels Gate the Integration Window, Plateau Potentials, and Induction of Synaptic Plasticity in Dorsal But Not Ventral CA1 Neurons. J Neurosci 37:3940-3955.
Malik R, Dougherty KA, Parikh K, Byrne C, Johnston D (2016) Mapping the electrophysiological and morphological properties of CA1 pyramidal neurons along the longitudinal hippocampal axis. Hippocampus 26:341-361.
Marder E, Taylor AL (2011) Multiple models to capture the variability in biological neurons and networks. Nat Neurosci 14:133-138.
Mateos-Aparicio P, Murphy R, Storm JF (2014) Complementary functions of SK and Kv7/M potassium channels in excitability control and synaptic integration in rat hippocampal dentate granule cells. J Physiol 592:669-693.
Mayford M, Siegelbaum SA, Kandel ER (2012) Synapses and memory storage. Cold Spring Harb Perspect Biol 4.
McHugh TJ, Jones MW, Quinn JJ, Balthasar N, Coppari R, Elmquist JK, Lowell BB, Fanselow MS, Wilson MA, Tonegawa S (2007) Dentate gyrus NMDA receptors mediate rapid pattern separation in the hippocampal network. Science 317:94-99.
Mishra P, Narayanan R (2015) High-conductance states and A-type K+ channels are potential regulators of the conductance-current balance triggered by HCN channels. Journal of neurophysiology 113:23-43.
Mishra P, Narayanan R (2019) Disparate forms of heterogeneities and interactions among them drive channel decorrelation in the dentate gyrus: Degeneracy and dominance. Hippocampus 29:378-403.
Mozzachiodi R, Byrne JH (2010) More than synaptic plasticity: role of nonsynaptic plasticity in learning and memory. Trends Neurosci 33:17-26.

Narayanan R, Johnston D (2007) Long-term potentiation in rat hippocampal neurons is accompanied by spatially widespread changes in intrinsic oscillatory dynamics and excitability. Neuron 56:1061-1075.
Narayanan R, Johnston D (2008) The h channel mediates location dependence and plasticity of intrinsic phase response in rat hippocampal neurons. J Neurosci 28:5846-5860.
Narayanan R, Johnston D (2010) The h current is a candidate mechanism for regulating the sliding modification threshold in a BCM-like synaptic learning rule. Journal of neurophysiology 104:1020-1033.
Narayanan R, Johnston D (2012) Functional maps within a single neuron. Journal of neurophysiology 108:2343-2351.
Narayanan R, Dougherty KJ, Johnston D (2010) Calcium Store Depletion Induces Persistent Perisomatic Increases in the Functional Density of h Channels in Hippocampal Pyramidal Neurons. Neuron 68:921-935.
Nelson SB, Turrigiano GG (2008) Strength through diversity. Neuron 60:477-482.
Neunuebel JP, Knierim JJ (2014) CA3 retrieves coherent representations from degraded input: direct evidence for CA3 pattern completion and dentate gyrus pattern separation. Neuron 81:416-427.
Neves G, Cooke SF, Bliss TV (2008) Synaptic plasticity, memory and the hippocampus: a neural network approach to causality. Nature reviews Neuroscience 9:65-75.
Nicolay NH, Hertle D, Boehmerle W, Heidrich FM, Yeckel M, Ehrlich BE (2007) Inositol 1,4,5 trisphosphate receptor and chromogranin B are concentrated in different regions of the hippocampus. Journal of neuroscience research 85:2026-2036.
O'Leary T, Williams AH, Caplan JS, Marder E (2013) Correlations in ion channel expression emerge from homeostatic tuning rules. Proc Natl Acad Sci U S A 110:E2645-2654.
O'Leary T, Williams AH, Franci A, Marder E (2014) Cell types, network homeostasis, and pathological compensation from a biologically plausible ion channel expression model. Neuron 82:809-821.
O'Mara SM, Rowan MJ, Anwyl R (1995) Metabotropic glutamate receptor-induced homosynaptic long-term depression and depotentiation in the dentate gyrus of the rat hippocampus in vitro. Neuropharmacology 34:983-989.
Pavlides C, Greenstein YJ, Grudman M, Winson J (1988) Long-term potentiation in the dentate gyrus is induced preferentially on the positive phase of theta-rhythm. Brain Res 439:383-387.
Pernia-Andrade AJ, Jonas P (2014) Theta-gamma-modulated synaptic currents in hippocampal granule cells in vivo define a mechanism for network oscillations. Neuron 81:140-152.
Pignatelli M, Ryan TJ, Roy DS, Lovett C, Smith LM, Muralidhar S, Tonegawa S (2019) Engram Cell Excitability State Determines the Efficacy of Memory Retrieval. Neuron 101:274-284 e275.
Poolos NP, Johnston D (2012) Dendritic ion channelopathy in acquired epilepsy. Epilepsia 53 Suppl 9:32-40.
Rao-Ruiz P, Yu J, Kushner SA, Josselyn SA (2019) Neuronal competition: microcircuit mechanisms define the sparsity of the engram. Current opinion in neurobiology 54:163-170.
Rathour RK, Narayanan R (2019) Degeneracy in hippocampal physiology and plasticity. Hippocampus In press:DOI: 10.1002/hipo.23139.

Rathour RK, Malik R, Narayanan R (2016) Transient potassium channels augment degeneracy in hippocampal active dendritic spectral tuning. Scientific reports 6:24678.
Reyes R, Lauritzen I, Lesage F, Ettaiche M, Fosset M, Lazdunski M (2000) Immunolocalization of the arachidonic acid and mechanosensitive baseline traak potassium channel in the nervous system. Neuroscience 95:893-901.
Rose CR, Konnerth A (2001) Stores not just for storage. intracellular calcium release and synaptic plasticity. Neuron 31:519-522.
Rosenkranz JA, Johnston D (2006) Dopaminergic regulation of neuronal excitability through modulation of Ih in layer V entorhinal cortex. J Neurosci 26:3229-3244.
Ross WN (2012) Understanding calcium waves and sparks in central neurons. Nature reviews Neuroscience 13:157-168.
Sahay A, Wilson DA, Hen R (2011) Pattern separation: a common function for new neurons in hippocampus and olfactory bulb. Neuron 70:582-588.
Sailer CA, Hu H, Kaufmann WA, Trieb M, Schwarzer C, Storm JF, Knaus HG (2002) Regional differences in distribution and functional expression of small-conductance Ca2+-activated K+ channels in rat brain. J Neurosci 22:9698-9707.
Sainsbury RS, Bland BH (1981) The effects of selective septal lesions on theta production in CA1 and the dentate gyrus of the hippocampus. Physiol Behav 26:1097-1101.
Sanchez-Alonso JL, Halliwell JV, Colino A (2008) ZD 7288 inhibits T-type calcium current in rat hippocampal pyramidal cells. Neuroscience letters 439:275-280.
Schmidt-Hieber C, Jonas P, Bischofberger J (2004) Enhanced synaptic plasticity in newly generated granule cells of the adult hippocampus. Nature 429:184-187.
Sehgal M, Song C, Ehlers VL, Moyer JR, Jr. (2013) Learning to learn - intrinsic plasticity as a metaplasticity mechanism for memory formation. Neurobiology of learning and memory 105:186-199.
Senzai Y, Buzsaki G (2017) Physiological Properties and Behavioral Correlates of Hippocampal Granule Cells and Mossy Cells. Neuron 93:691-704 e695.
Sharp AH, McPherson PS, Dawson TM, Aoki C, Campbell KP, Snyder SH (1993) Differential immunohistochemical localization of inositol 1,4,5-trisphosphate- and ryanodine-sensitive Ca2+ release channels in rat brain. J Neurosci 13:3051-3063.
Shors TJ, Dryver E (1994) Effect of stress and long-term potentiation (LTP) on subsequent LTP and the theta burst response in the dentate gyrus. Brain Res 666:232-238.
Song JH, Huang CS, Nagata K, Yeh JZ, Narahashi T (1997) Differential action of riluzole on tetrodotoxin-sensitive and tetrodotoxin-resistant sodium channels. The Journal of pharmacology and experimental therapeutics 282:707-714.
Srikanth S, Narayanan R (2015) Variability in State-Dependent Plasticity of Intrinsic Properties during Cell-Autonomous Self-Regulation of Calcium Homeostasis in Hippocampal Model Neurons. eNeuro 2:e0053-0015.2015.
Stegen M, Young CC, Haas CA, Zentner J, Wolfart J (2009) Increased leak conductance in dentate gyrus granule cells of temporal lobe epilepsy patients with Ammon's horn sclerosis. Epilepsia 50:646-653.
Stegen M, Kirchheim F, Hanuschkin A, Staszewski O, Veh RW, Wolfart J (2012) Adaptive intrinsic plasticity in human dentate gyrus granule cells during temporal lobe epilepsy. Cerebral cortex 22:2087-2101.
Surges R, Kukley M, Brewster A, Ruschenschmidt C, Schramm J, Baram TZ, Beck H, Dietrich D (2012) Hyperpolarization-activated cation current Ih of dentate gyrus granule cells is

upregulated in human and rat temporal lobe epilepsy. Biochemical and biophysical research communications 420:156-160.
Terzic A, Perez-Terzic C (2010) Channelopathies: decoding disease pathogenesis. Science translational medicine 2:42ps37.
Titley HK, Brunel N, Hansel C (2017) Toward a Neurocentric View of Learning. Neuron 95:19-32.
Tonegawa S, Morrissey MD, Kitamura T (2018) The role of engram cells in the systems consolidation of memory. Nature reviews Neuroscience 19:485-498.
Turrigiano G (2011) Too many cooks? Intrinsic and synaptic homeostatic mechanisms in cortical circuit refinement. Annu Rev Neurosci 34:89-103.
Urbani A, Belluzzi O (2000) Riluzole inhibits the persistent sodium current in mammalian CNS neurons. The European journal of neuroscience 12:3567-3574.
Wang Y, Wu J, Rowan MJ, Anwyl R (1996) Ryanodine produces a low frequency stimulation-induced NMDA receptor-independent long-term potentiation in the rat dentate gyrus in vitro. The Journal of physiology 495 (Pt 3):755-767.
Winson J (1974) Patterns of hippocampal theta rhythm in the freely moving rat. Electroencephalogr Clin Neurophysiol 36:291-301.
Winson J (1978) Loss of hippocampal theta rhythm results in spatial memory deficit in the rat. Science 201:160-163.
Yarishkin O, Lee DY, Kim E, Cho CH, Choi JH, Lee CJ, Hwang EM, Park JY (2014) TWIK-1 contributes to the intrinsic excitability of dentate granule cells in mouse hippocampus. Molecular brain 7:80.
Yim MY, Hanuschkin A, Wolfart J (2015) Intrinsic rescaling of granule cells restores pattern separation ability of a dentate gyrus network model during epileptic hyperexcitability. Hippocampus 25:297-308.
Yiu AP, Mercaldo V, Yan C, Richards B, Rashid AJ, Hsiang HL, Pressey J, Mahadevan V, Tran MM, Kushner SA, Woodin MA, Frankland PW, Josselyn SA (2014) Neurons are recruited to a memory trace based on relative neuronal excitability immediately before training. Neuron 83:722-735.
Young CC, Stegen M, Bernard R, Muller M, Bischofberger J, Veh RW, Haas CA, Wolfart J (2009) Upregulation of inward rectifier K+ (Kir2) channels in dentate gyrus granule cells in temporal lobe epilepsy. The Journal of physiology 587:4213-4233.
Zhang W, Linden DJ (2003) The other side of the engram: experience-driven changes in neuronal intrinsic excitability. Nature reviews Neuroscience 4:885-900.

FIGURE LEGENDS

Figure 1: Illustration of theta burst firing inducing contrasting changes in sub- *vs.* supra-threshold excitability in a dentate gyrus granule cell. *A,* Illustration showing whole-cell patch clamp recording from a dentate gyrus granule cell. *B*, Experimental protocol, illustrating initial recordings of basic measurements after establishing a patch in whole-cell current-clamp configuration followed by five minutes recording of baseline measurements (*VI* and *fI* curves followed by alpha summation; shown in black) using chirp stimulus (*top*). After establishing 5 min of stable baseline, theta-patterned current pulses were injected into the neuron to elicit theta burst firing (TBF). Neuronal response properties were monitored for a further 40 minutes employing the chirp stimulus. At the end of 40 minutes, same sets of basic measurements (*VI* and *fI* curves followed by alpha summation; shown in red) were recorded to compare them with their baseline counterparts. A large 100-pA hyperpolarizing current pulse was provided before the chirp current to estimate input resistance ($\bar{R}_{\mathrm{in}}$) and to observe and correct series resistance changes through the course of the experiment. *C*, Membrane voltage (*top*) recorded from the example granule cell in response to the theta-patterned current injection (*bottom*), showing 50 action potential elicited during a theta burst firing (TBF) pattern. This train was repeated thrice with 10 s inter-train intervals to form the TBF protocol employed in this study. *D*, Voltage responses of an example neuron to 700 ms current pulses of amplitude varying from –25 pA to +25 pA (in steps of 5 pA), before (black) and 40 mins after (red) TBF. Input resistance (R_{in}) was calculated as the slope of the plot depicting steady-state voltage response as a function of the injected current amplitude. Inset represents the temporal evolution of input resistance estimate ($\bar{R}_{\mathrm{in}}$) from neuronal response to the single hyperpolarizing pulse (depicted in panel *B*). *E*, Voltage responses of the example neuron to the chirp current before (black: 0–5 min average)

and 40 mins after (red: 40–45 min average) TBF. *F*, Impedance amplitude computed from the current stimulus shown in panel *B* (*top*) and the voltage responses shown in panel *E*. $|Z|_{max}$ represents the maximum impedance amplitude, Q is resonance strength and f_R denotes resonance frequency. *G*, Voltage responses of the example neuron to 5 alpha-current injections arriving at 20 Hz, recorded before (black) and 40 mins after (red) TBF. Temporal summation ratio (S_α) was computed as the ratio of the amplitude of the fifth response to that of the first. *H*, Voltage response of the example neuron to a 700-ms current pulse of 250 pA, before (black) and 40 mins after (red) TBF. *I*, Frequency of action potential firing plotted as a function of injected current amplitude for the example cell. Note that these are firing frequencies converted from the number of spikes for the 700-ms injection duration. All traces and measurements shown in this example are from a single experiment.

Figure 2. **Theta burst firing induced contrasting changes in sub- *vs.* supra-threshold excitability in dentate gyrus granule cells.** For all panels, the Control (black) group (n=10) corresponds to experiments where no protocol was applied through the 45-min period of the experiment, and TBF (red) group (n=32) is for neurons subjected to theta burst firing. For the TBF group, "Baseline" measurements were obtained before TBF and "TBF" measurements were after TBF. *A*, Population data representing change in input resistance (R_{in}) at the beginning (*empty circles*) and the end (*filled circles*) of the experiment. *B,* Temporal evolution of percentage change in input resistance estimate ($\bar{R}_{in}$; Mean ± SEM). *C,* Normalized count of neurons from panel *A* plotted as functions of percentage change in R_{in} both for control and TBF case. *D–E*, Same as *A–B*, representing impedance amplitude ($|Z|_{max}$). *F*, Frequency of firing plotted as a function of injected current amplitude for both groups. *: p<0.05; **: p<0.005. Student's t test. *G*, Plots comparing percentage change in various measurements from their initial

values to end of experiment values, for both control and TBF experiments. The list of symbols and corresponding measurements is enumerated in Table 1. The Wilcoxon signed rank test was used for *p* value calculation in panels *A* and *D*, for comparing measurements from the same set of cells. The Wilcoxon rank sum test was employed for *p* value calculation in panel *G*, to compare percentage changes in the control group *vs*. those in the TBF group.

Figure 3. **Differential pair-wise correlations among TBF-induced changes in thirteen electrophysiological measurements.** *A*, Pair-wise scatter plot matrices of TBF-induced changes in 13 sub- and supra-threshold measurements recorded from granule cells (n=20). These scatter plot matrices are overlaid on the corresponding color-coded correlation matrices. The bottom most row presents the histogram of percentage change for corresponding measurements spanning their respective ranges. The list of symbols and corresponding measurements is enumerated in Table 1. *B*, Distribution of correlation coefficient values for 13 measurements corresponding to the pair-wise scatter plots shown in panel *A*.

Figure 4. **Analyses of changes in steady-state and frequency-dependent measurements point to HCN channels as a candidate mechanism behind TBF-induced reduction in sub-threshold excitability.** *A,* Percentage changes in impedance amplitude as a function of frequency for Control (no protocol) and TBF groups. In the control group, the percentage changes were computed as the change in impedance amplitude measured at 45-min, compared to the initial measurements. In the TBF group, the percentage changes are between those measured before and 40 mins after TBF. *B,* Quantification of percentage changes in $|Z|$ within three frequency bands (0–5 Hz, 5–10 Hz and 10–15 Hz). The value for each neuron were computed as the area under the curve (AUC) of percentage change in $|Z|$. *Left,* Plot showing the quartiles of

AUC of percentage change in $|Z|$ for neurons in the TBF group. The symbol "#" refers to the outcomes of Wilcoxon rank sum test on whether TBF-induced changes in $|Z|$ within that frequency band were significantly different from zero. #: $p<0.05$; ##: $p<0.001$. The symbol "*" refers to the outcomes of Wilcoxon signed rank test, assessing whether TBF-induced changes in $|Z|$ across the different frequency bands were significantly different from one another. **: $p<0.001$. *Right,* Plot showing the quartiles of AUC of percentage change in $|Z|$ for neurons in the Control and TBF groups. The symbol "*" refers to the outcomes of Wilcoxon rank sum test, assessing whether TBF-induced changes in $|Z|$ within each frequency band were significantly different between the Control and the TBF groups. *: $p<0.05$; **: $p<0.005$. Note that for the Control group, changes in $|Z|$ within none of the three frequency bands were significantly different from zero, or significantly different from one another. Note that the representation has been split into two separate graphs to avoid clutter of symbols denoting statistical test outcomes. *C,* Voltage responses of an example neuron to 700 ms current pulses of amplitude varying from –25 pA to +25 pA (in steps of 5 pA), recorded before (*Baseline*) and 40 mins after TBF. The responses colored blue and green are for positive and negative current injections, respectively. Input resistance values, computed from depolarizing (R_{in}^{+}) and hyperpolarizing (R_{in}^{-}) responses, were slopes of the plots depicting steady-state voltage responses as functions of positive and negative current injections, respectively (*bottom*). R_{in}^{+} and R_{in}^{-} were calculated for traces obtained before (open circles) and after (closed circles) TBF (*bottom*). *D*, Population level analysis to quantify percentage changes (at the end of experiment, compared to the measurement at the beginning) in R_{in}^{+} (blue) and R_{in}^{-} (green) independently for Control (n=8) and TBF (n=28) experiments. The p values presented for comparisons within each group (either Control or TBF)

correspond to Wilcoxon signed rank test and *p* values across groups are for Wilcoxon rank sum test.

Figure 5. **Activity-dependent reduction in sub-threshold excitability was blocked in the presence of ZD7288, a HCN channel blocker.** For all panels, the ZD Control (black) group (n=8) corresponds to experiments where no protocol was applied through the 45-min period of the experiment, and ZD TBF (red) group (n=12) is for neurons subjected to theta burst firing. For the ZD TBF group, "Baseline" measurements were obtained before TBF and "TBF" measurements were after TBF. All experiments reported in this figure were performed in the presence of 20 μM ZD7288 in the bath and in the pipette solution. *A*, Population data representing change in input resistance (R_{in}) at the beginning (*empty circles*) and the end (*filled circles*) of the experiment. *B,* Temporal evolution of percentage change in input resistance estimate ($\bar{R}_{in}$; Mean ± SEM). *C,* Normalized count of neurons from panel *A* plotted as functions of percentage change in R_{in}. *D–E*, Same as *A–B*, representing impedance amplitude ($|Z|_{max}$). *F*, Frequency of firing plotted as a function of injected current amplitude for both groups. *: p<0.05; **: p<0.005. Student's *t* test. *G*, Plots comparing percentage change in various measurements from their initial values to end of experiment values. The list of symbols and corresponding measurements is enumerated in Table 1. The Wilcoxon signed rank test was used for *p* value calculation in panels *A* and *D*, for comparing measurements from the same set of cells. The Wilcoxon rank sum test was employed for *p* value calculation in panel *G*, to compare percentage changes in the control group *vs*. those in the TBF group.

Figure 6. **Acute treatment with Riluzole, a persistent sodium channel blocker, reduced the firing rate of DG granule cells without altering their sub-threshold physiological**

characteristics. *A, Right*, Voltage responses of a DG granule cell to 700 ms current pulses of amplitude varying from –25 pA to +25 pA (in steps of 5 pA), with normal ACSF (*black*) and in the presence of Riluzole in the bath (*blue*). *Left*, Input resistance (R_{in}) was calculated as the slope of the *V–I* plot depicting steady-state voltage response as a function of the injected current amplitude. *B,* Voltage response of the example neuron to 5 alpha-current injections arriving at 20 Hz, depicting temporal summation. Temporal summation ratio (S_α) was computed as the ratio of the amplitude of the fifth response to that of the first. *C*, *Top,* Voltage response of the example neuron to a 700-ms current pulse of 250 pA in ACSF (*black*) and in the presence of riluzole (*blue*). *Bottom*, Frequency of firing plotted as a function of injected current amplitude for the example cell. Note that these are firing frequencies converted from the number of spikes obtained for 700-ms duration pulses. *D*, *Left*, Voltage responses of the example neuron to the chirp current (Fig. 1*B*) in ACSF (*black*) and in the presence of Riluzole (*blue*). *Right*, Impedance amplitude computed from the current stimulus shown in Fig 1*B* (*top*) and the voltage responses shown in panel *D*. $|Z|_{max}$ represents the maximum impedance amplitude, *Q* is resonance strength and resonance frequency is represented by f_R. *E–L*, Population data of measurements from all DG granule cells recorded before and after adding riluzole to the bath: RMP (*E*); input resistance, R_{in} (*F*); membrane potential dependence of input resistance (*G*); temporal summation (*H*); impedance amplitude, $|Z|_{max}$ (*I*) and its voltage dependence (*J*); firing rate at 0–250 pA current injection (*K*) and for 250 pA current injection (*L*). For panel *K*, statistical comparisons were performed with paired Student's *t* test; *: $p < 0.05$.

Figure 7. **Activity-dependent intrinsic plasticity was blocked by Riluzole, a persistent sodium channel blocker.** For all panels, the Riluzole Control (black) group (n=10) corresponds to experiments where no protocol was applied through the 45-min period of the experiment, and

Riluzole TBF (red) group (n=10) is for neurons subjected to theta burst firing. For the Riluzole TBF group, "Baseline" measurements were obtained before TBF and "TBF" measurements were after TBF. All experiments reported in this figure were performed in the presence of 20 μM Riluzole in the bath. *A*, Population data representing change in input resistance (R_{in}) at the beginning (*empty circles*) and the end (*filled circles*) of the experiment. *B,* Temporal evolution of percentage change in input resistance estimate ($\bar{R}_{in}$; Mean ± SEM). *C,* Normalized count of neurons from panel *A* plotted as a function of percentage change in R_{in}. *D–F*, Same as *A–C*, representing impedance amplitude ($|Z|_{max}$). *G*, Frequency of firing plotted as a function of injected current amplitude for both groups. *: p<0.05; **: p<0.005. Student's t test. *H*, Plots comparing percentage change in various sub-threshold measurements from their initial values to end of experiment values. The list of symbols and corresponding measurements are enumerated in Table 1. The Wilcoxon signed rank test was used for p value calculation in panels *A* and *D*, for comparing measurements from the same set of cells. The Wilcoxon rank sum test was employed for p value calculation in panel *G*, to compare percentage changes in the control group *vs*. those in the TBF group.

Figure 8. **Activity-dependent intrinsic plasticity was blocked by BAPTA, a fast calcium chelator.** For all panels, the BAPTA Control (black) group (n=14) corresponds to experiments where no protocol was applied through the 45-min period of the experiment, and BAPTA TBF (red) group (n=13) is for neurons subjected to theta burst firing. For the BAPTA TBF group, "Baseline" measurements were obtained before TBF and "TBF" measurements were after TBF. All experiments reported in this figure were performed in the presence of 30 mM BAPTA in the pipette solution. *A*, Population data representing change in input resistance (R_{in}) at the beginning (*empty circles*) and the end (*filled circles*) of the experiment. *B,* Normalized count of neurons

from panel *A* plotted as functions of percentage change in R_{in}. *C–D*, Same as *A–B*, representing impedance amplitude ($|Z|_{max}$). *E*, Frequency of firing plotted as a function of injected current amplitude for both groups. *: $p<0.05$; **: $p<0.005$. Student's *t* test. *F*, Plots comparing percentage change in various sub-threshold measurements from their initial values to end of experiment values. The list of symbols and corresponding measurements are enumerated in Table 1. The Wilcoxon signed rank test was used for *p* value calculation in panels *A* and *C*, for comparing measurements from the same set of cells. The Wilcoxon rank sum test was employed for *p* value calculation in panel *G*, to compare percentage changes in the control group *vs*. those in the TBF group.

Figure 9. **Activity-dependent expression of intrinsic plasticity was independent of synaptic receptors.** For all panels, the "Syn Block" (blue) group (n=11) corresponds to experiments where neurons were subjected the TBF protocol in the presence of synaptic blockers (AMPAR, $GABA_AR$ and $GABA_BR$). The "AP5" (blue) group (n=12) corresponds to experiments where neurons were subjected the TBF protocol in the presence of AP5, an NMDAR antagonist. These are compared with the TBF group where normal ACSF was employed. For all groups, "Baseline" measurements were obtained before TBF and "TBF" measurements were after TBF. *A*, Population data representing change in input resistance (R_{in}) at the beginning (*empty circles*) and the end (*filled circles*) of the experiment. *B,* Temporal evolution of percentage change in input resistance estimate ($\bar{R}_{in}$; Mean ± SEM). *C,* Normalized count of neurons from the three groups plotted as functions of percentage change in R_{in}. *D–E*, Same as *A–B*, representing impedance amplitude ($|Z|_{max}$). *F*, Frequency of firing plotted as a function of injected current amplitude for all three groups. *: $p<0.05$; **: $p<0.005$. Student's *t* test. *G*, Plots comparing percentage change in various sub-threshold measurements from their initial values to end of

experiment values. The list of symbols and corresponding measurements are enumerated in Table 1. The Wilcoxon signed rank test was used for *p* value calculation in panels *A* and *D*, for comparing measurements from the same set of cells. The Wilcoxon rank sum test was employed for *p* value calculation in panel *G*, to compare percentage changes in the control group *vs*. those in the TBF group.

Figure 10. **Activity-dependent intrinsic plasticity was blocked by Nimodipine, a *L*-type calcium channel blocker.** For all panels, the Nimodipine Control (black) group (n=6) corresponds to experiments where no protocol was applied through the 45-min period of the experiment, and Nimodipine TBF (red) group (n=13) is for neurons subjected to theta burst firing. For the Nimodipine TBF group, "Baseline" measurements were obtained before TBF and "TBF" measurements were after TBF. All experiments reported in this figure were performed in the presence of 10 μM Nimodipine in the ACSF bath solution. *A*, Population data representing change in input resistance (R_{in}) at the beginning (*empty circles*) and the end (*filled circles*) of the experiment. *B,* Temporal evolution of percentage change in input resistance estimate ($\overline{?}_{in}$; Mean ± SEM). *C,* Normalized count of neurons from panel *A* plotted as a function of percentage change in R_{in}. *D–E*, Same as *A–B*, representing impedance amplitude ($|Z|_{max}$). *F*, Frequency of firing plotted as a function of injected current amplitude for both groups. *: p<0.05. Student's *t* test. *G*, Plots comparing percentage change in various sub-threshold measurements from their initial values to end of experiment values. The list of symbols and corresponding measurements is enumerated in Table 1. The Wilcoxon signed rank test was used for *p* value calculation in panels *A* and *D*, for comparing measurements from the same set of cells. The Wilcoxon rank sum test was employed for *p* value calculation in panel *G*, to compare percentage changes in the control group *vs*. those in the TBF group.

Figure 11. **Activity-dependent intrinsic plasticity was blocked by Heparin, an $InsP_3R$ blocker.** For all panels, the Heparin Control (black) group (n=10) corresponds to experiments where no protocol was applied through the 45-min period of the experiment, and Heparin TBF (red) group (n=9) is for neurons subjected to theta burst firing. For the Heparin TBF group, "Baseline" measurements were obtained before TBF and "TBF" measurements were after TBF. All experiments reported in this figure were performed in the presence of 1 mg/mL Heparin in the pipette. *A*, Population data representing change in input resistance (R_{in}) at the beginning (*empty circles*) and the end (*filled circles*) of the experiment. *B,* Temporal evolution of percentage change in input resistance estimate ($\bar{R}_{in}$; Mean ± SEM). *C,* Normalized count of neurons from panel *A* plotted as a function of percentage change in R_{in}. *D–E*, Same as *A–B*, representing impedance amplitude ($|Z|_{max}$). *F*, Frequency of firing plotted as a function of injected current amplitude for both groups. *: p<0.05. Student's t test. *G*, Plots comparing percentage change in various sub-threshold measurements from their initial values to end of experiment values. The list of symbols and corresponding measurements are enumerated in Table 1. The Wilcoxon signed rank test was used for p value calculation in panels *A* and *D*, for comparing measurements from the same set of cells. The Wilcoxon rank sum test was employed for p value calculation in panel *G*, to compare percentage changes in the control group *vs*. those in the TBF group.

Table 1: Sub- and supra-threshold physiological properties measured before and 40 minutes after TBF. These statistics correspond to the data plotted in Fig. 2. *p* values correspond to paired Student's *t* test, and data are represented as mean ± SEM.

	Measurement (units)	Before TBF	After TBF	Significance
Sub-threshold measurements				
1	Resting membrane potential, V_{RMP} (mV)	–75.9 ± 0.6	–72.3 ± 1.2	p=6.3×10^{-4}
2	Input resistance, R_{in} (MΩ)	141.8 ± 7.5	118.2 ± 8.02	p=4.4×10^{-6}
3	Maximal impedance amplitude, $\lvert Z\rvert_{max}$ (MΩ)	155.9 ± 8.2	134.2 ± 8.8	p=1.4×10^{-5}
4	Resonance frequency, f_R (Hz)	0.77 ± 0.01	0.99 ± 0.20	p = 0.27
5	Resonance strength, Q	1.03 ± 0.03	1.03 ± 0.003	p = 0.86
6	Total inductive phase, Φ_L (rad.Hz)	0.01 ± 0.002	0.01 ± 0.001	p = 0.33
7	Sag (%)	2.6 ± 0.14	3.3 ± 0.31	p=0.037
8	Summation ratio of αEPSPs, S_α	1.3 ± 0.03	1.23 ± 0.02	p=3.5×10^{-3}
Supra-threshold measurements				
1	Firing frequency	Significant increase after TBF		Fig. 2*F*
2	AP threshold, V_{th} (mV)	–38.9 ± 0.6	–42.9 ± 1.4	p=5.4×10^{-4}
3	AP peak, V_{AP}^{peak} (mV)	51.0 ± 1.7	43.2 ± 1.7	p=2.2×10^{-5}
4	AP amplitude, V_{AP} (mV)	126.2 ± 1.8	118.4 ± 1.9	p=2.0×10^{-5}
5	AP half-width, T_{APHW} (ms)	0.85 ± 0.02	0.82 ± 0.02	p=0.17
6	Peak dV/dt, $\left.\frac{dV}{dt}\right\|_{AP}^{max}$ (V/s)	528.5 ± 22.7	443.5 ± 20.8	p=9.6×10^{-4}
7	Min dV/dt, $\left.\frac{dV}{dt}\right\|_{AP}^{min}$ (V/s)	–125.2 ± 3.3	–128.3 ± 3.6	p=0.31
8	Latency to first spike, T_{1AP} (ms)	54.7 ± 5.6	49.2 ± 10.7	p=0.44
9	First ISI, T_{1ISI} (ms)	38.1 ± 9	8.5 ± 1.62	p=5.0×10^{-3}

SUPPLEMENTARY FIGURE LEGENDS

Supplementary Figure S1. Contrasting plasticity in sub- *vs.* supra-threshold excitability was observed when measurements were recorded at respective resting membrane potentials. *A,* Population data of resting membrane potential from all DG granule cells recorded before (black) and 40 mins after (red) TBF protocol, showing persistent changes in RMP after TBF. *B–C,* Population data of measurements from all DG granule cells recorded before (black) and 40 mins after (red) TBF protocol. Measurements were performed at the respective resting membrane potentials (shown in panel *A* for each cell), with zero current injection. Input resistance obtained from the *V–I* plot reduced after TBF (B), whereas firing rate increased (C). The Wilcoxon signed rank test was employed for *p* value calculation in panels *A–B*, and Student's *t* test was employed for *p* value calculation in panel *C*. *: $p<0.05$.

Supplementary Figure S2. Weak correlations between heterogeneities in TBF-induced plasticity and heterogeneities in intrinsic properties of DG granule cells. *A–C,* Population data representing TBF-induced change in input resistance plotted against resting membrane potential of the cells (*A*); input resistance of the cells (*B*); and firing rate of the cells in response to 250 pA current injection (*C*). *D–F*, Same as *A–C*, but with TBF-induced change in firing rate at 250 pA on the ordinate. Pearson correlation coefficient (*R*) is provided for each panel.

Supplementary Figure S3. Impact of acute treatment with Riluzole, a persistent sodium channel blocker, on several sub-threshold and action potential measurements of DG granule cells. *A–M,* Population data of measurements from all DG granule cells recorded before (black) and after (blue) adding riluzole to the bath: Sag ratio (*A*) and its voltage dependence (*B*); resonance frequency (*C*) and its voltage dependence (*D*); resonance strength (*E*) and its voltage

dependence (*F*); AP peak voltage (*G*); AP amplitude (*H*); AP threshold (*I*); AP half width (*J*); latency to first spike (*K*); peak (*L*) and minimum (*M*) dV/dt of the action potential waveform. Although there was a trend of consistent reduction in AP amplitude and AP peak voltage, none of the measurements depicted in this figure were statistically significant with Wilcoxon signed rank test. *N*, Membrane voltage (*top*) recorded from the example granule cell in response to the theta-patterned current injection (*bottom*) in the presence of riluzole in the ACSF, showing 50 action potential elicited during a theta burst firing (TBF) pattern. Similar to other cases, this train was repeated thrice (total 150 action potentials) with 10 s inter-train intervals to form the TBF protocol.

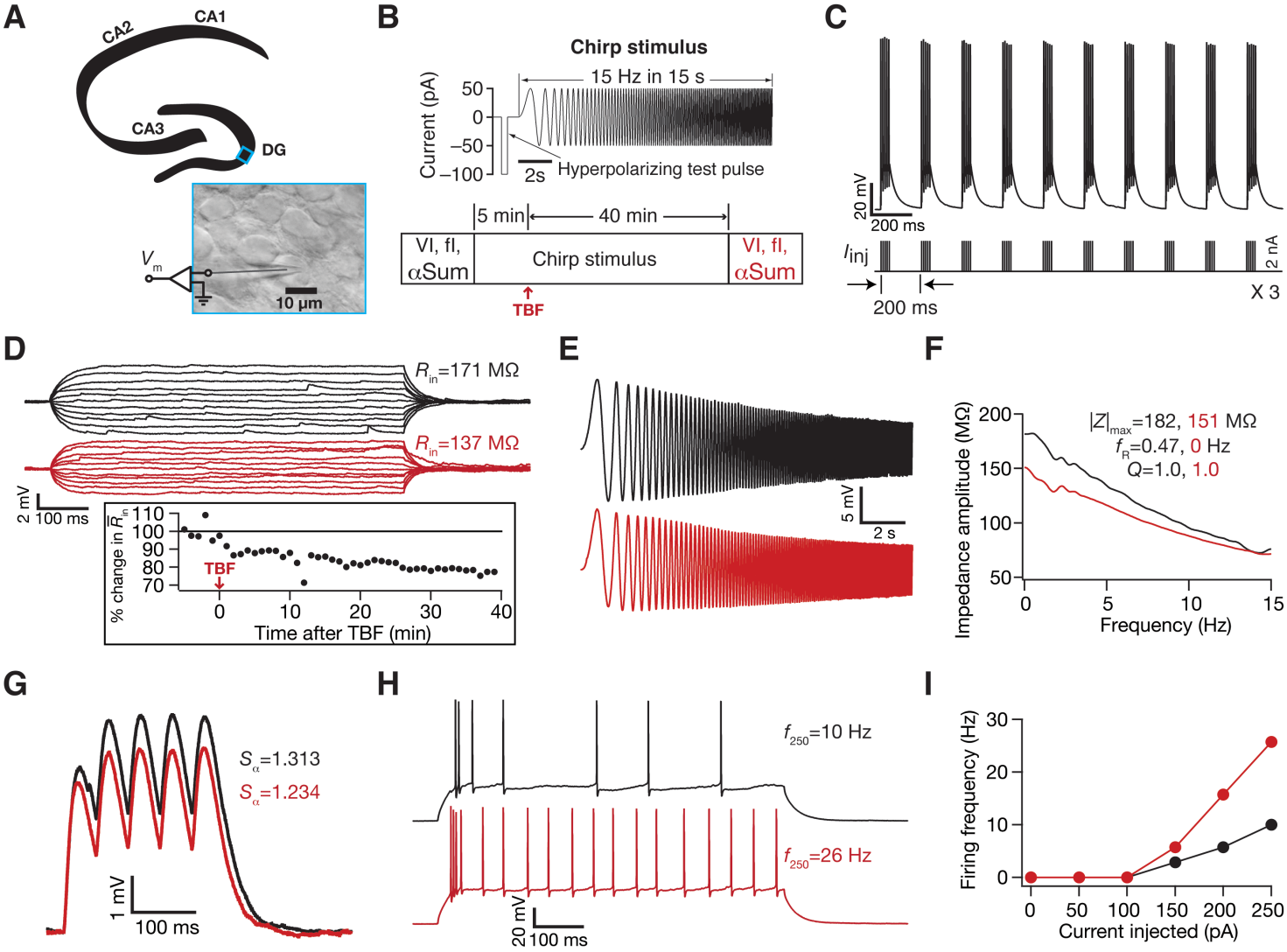

Mishra and Narayanan, Figure 1

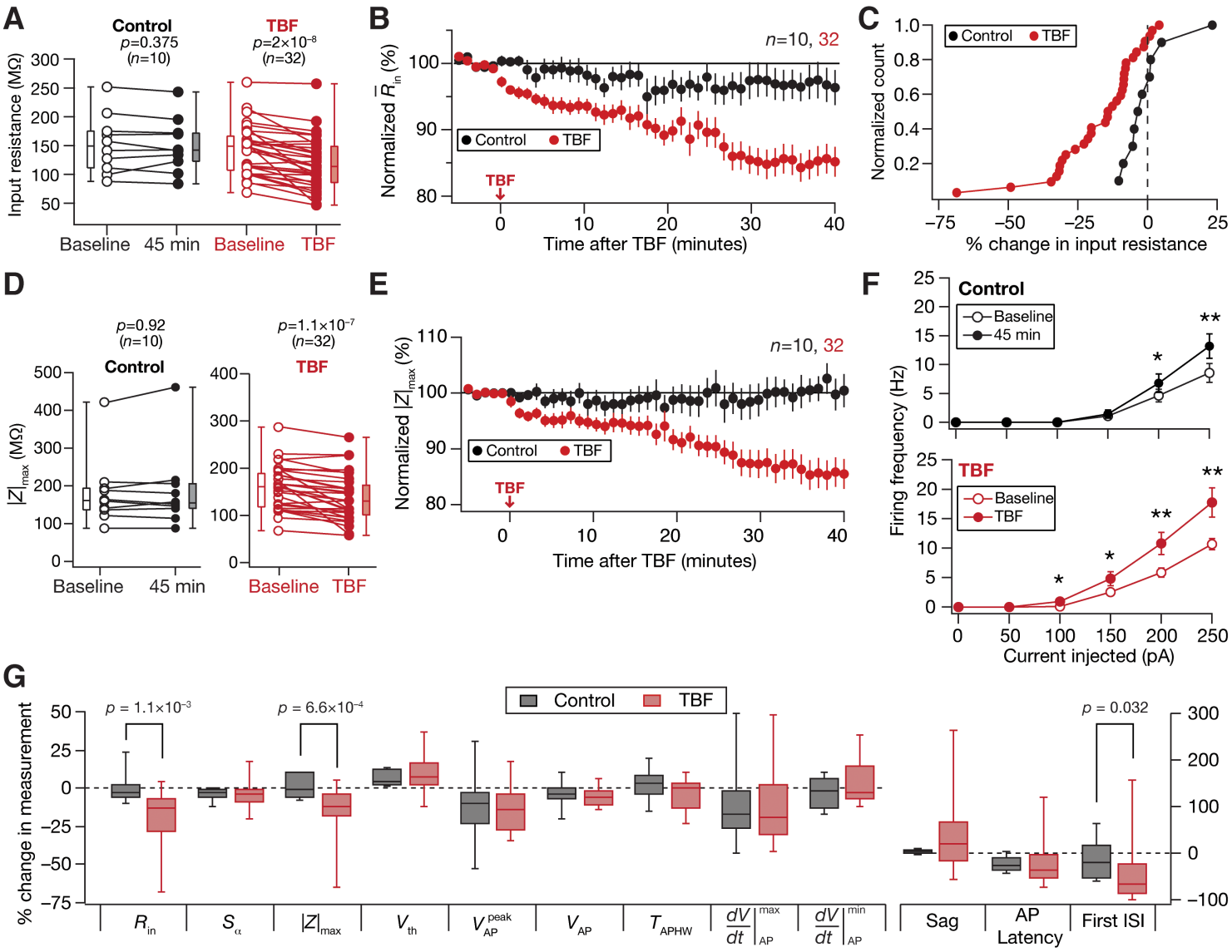

Mishra and Narayanan, Figure 2

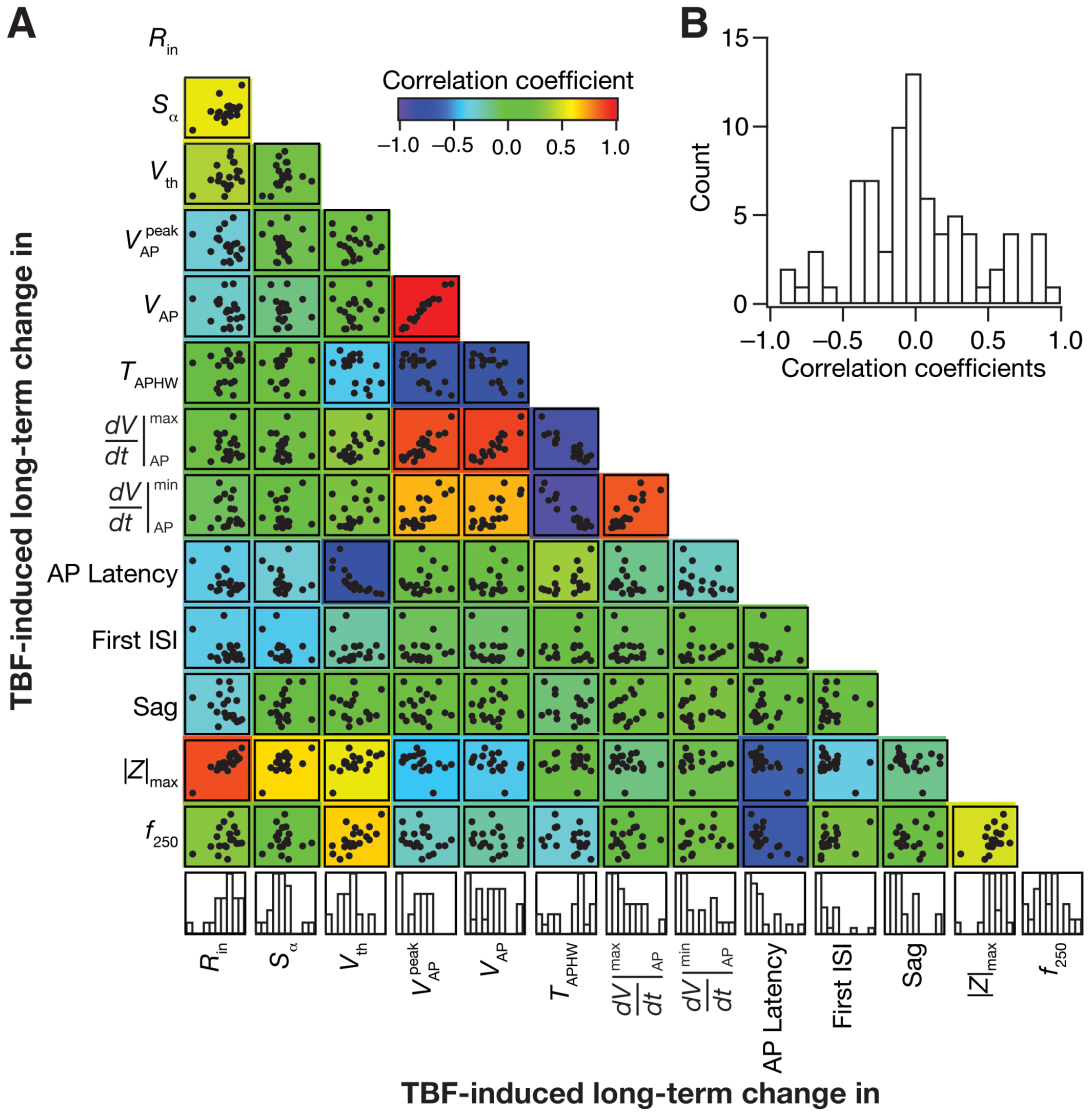

Mishra and Narayanan, Figure 3

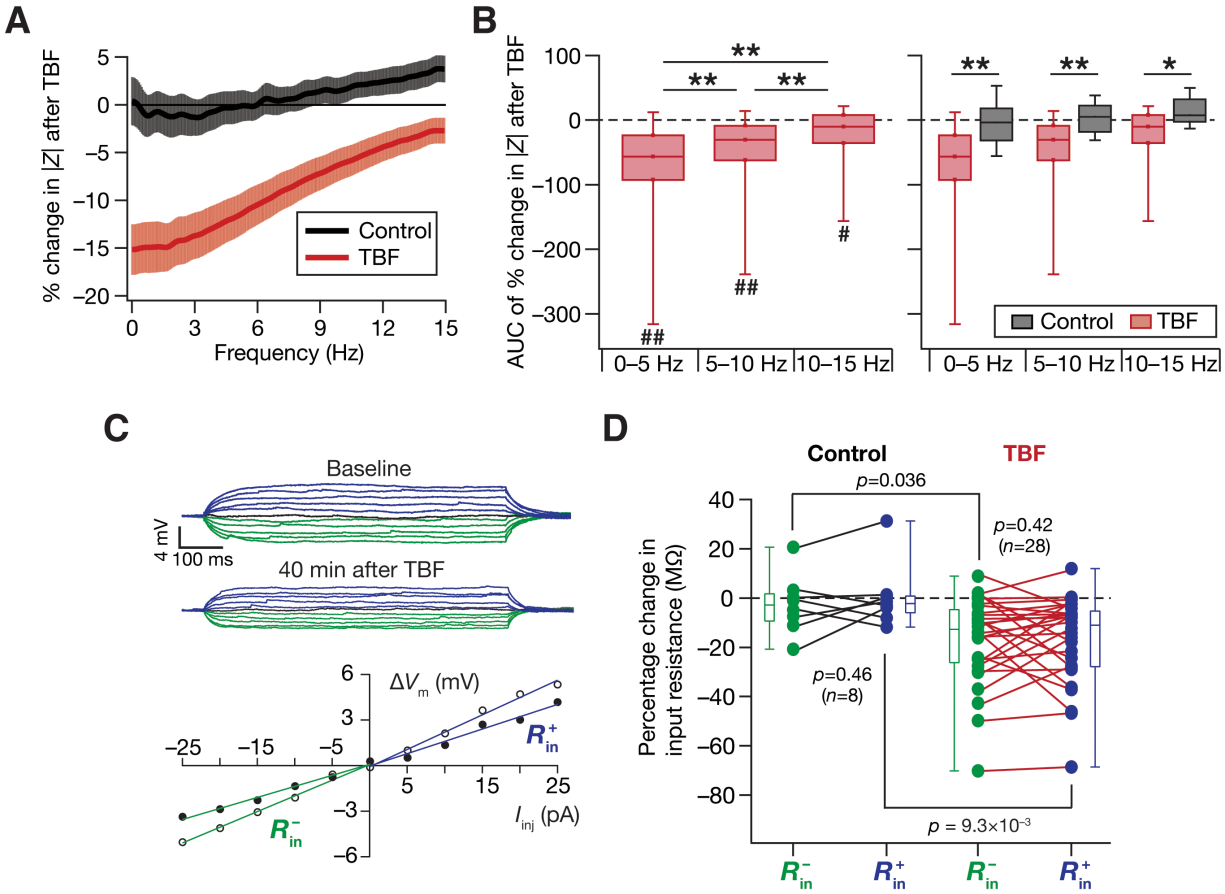

Mishra and Narayanan, Figure 4

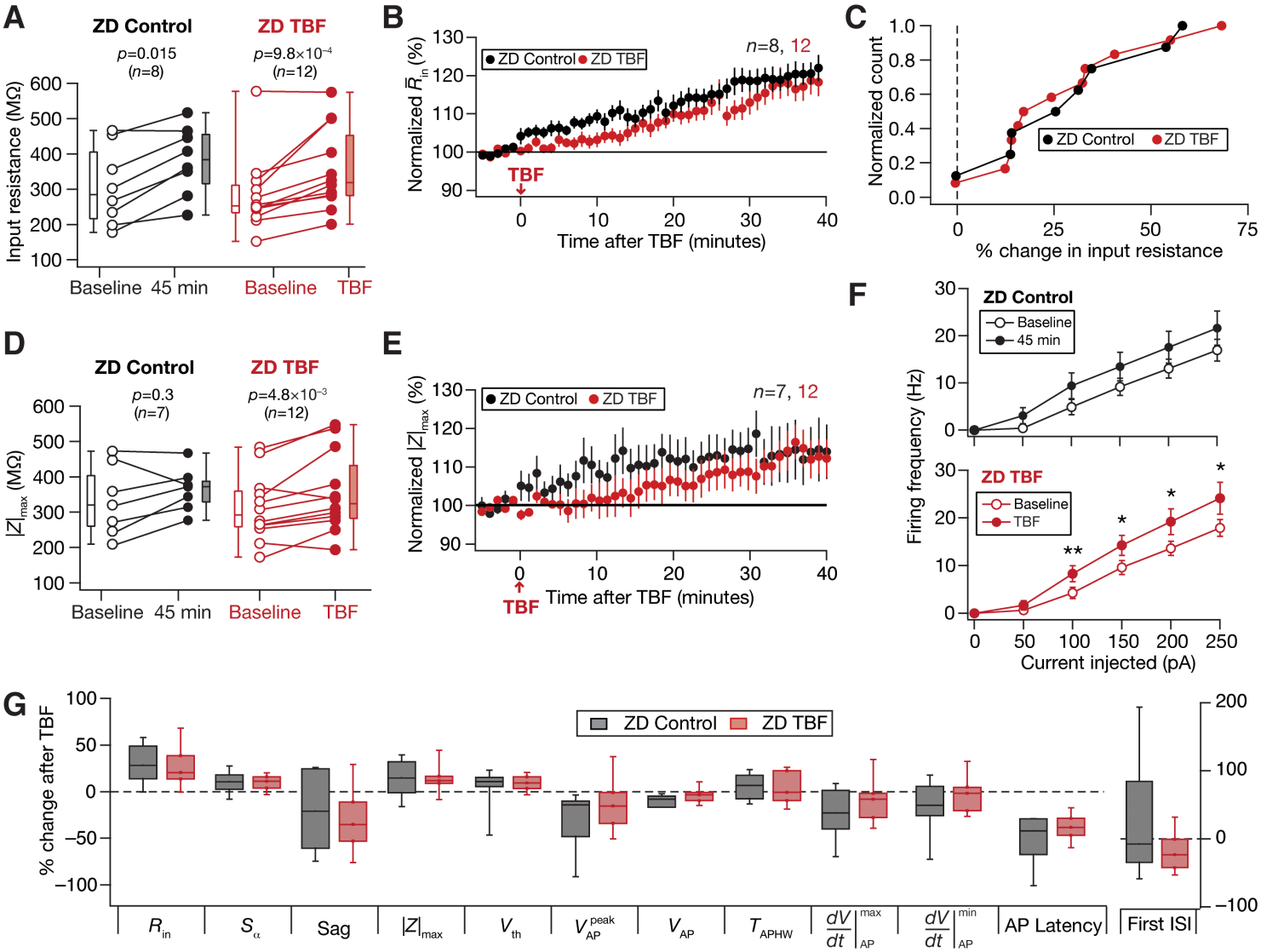

Mishra and Narayanan, Figure 5

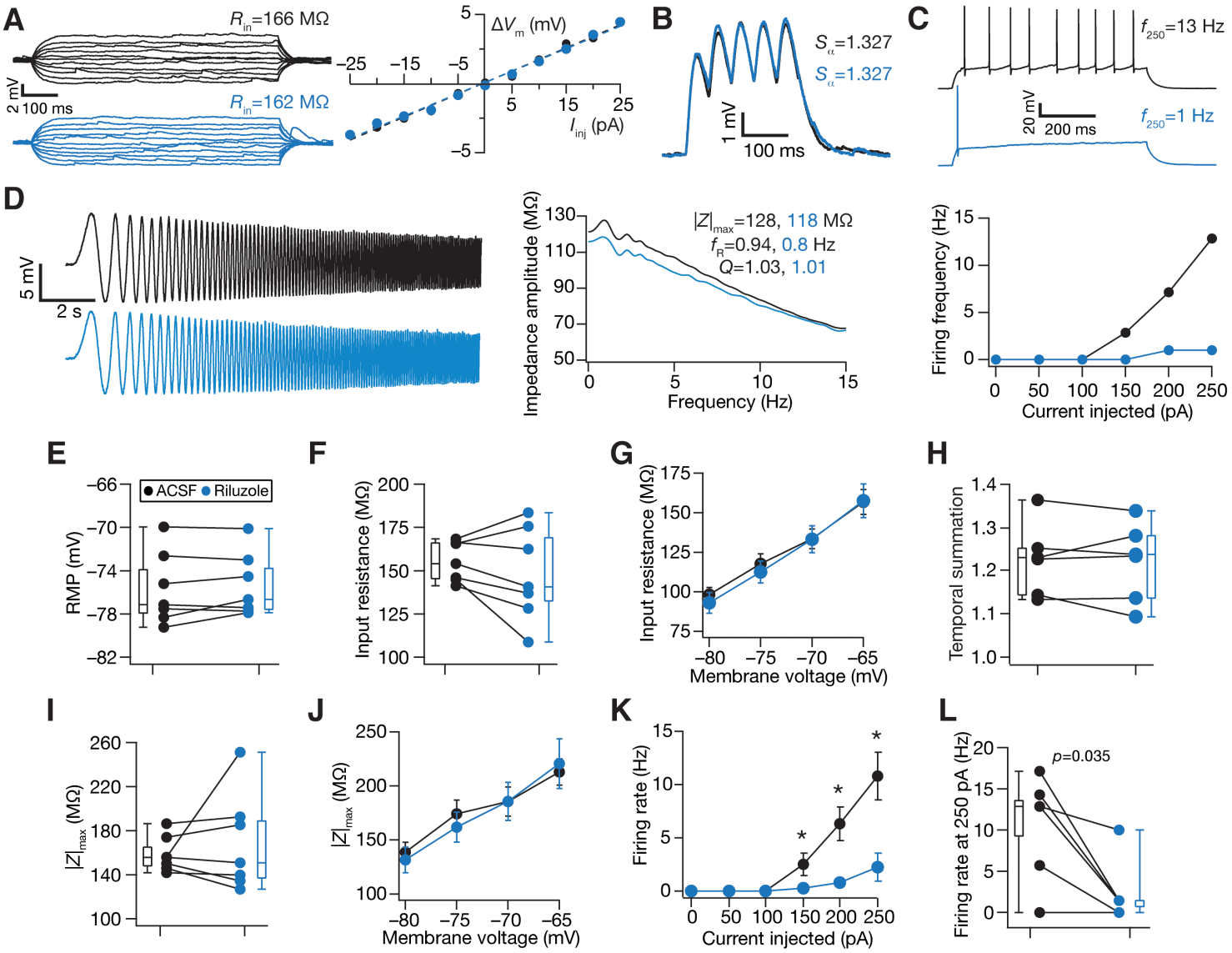

Mishra and Narayanan, Figure 6

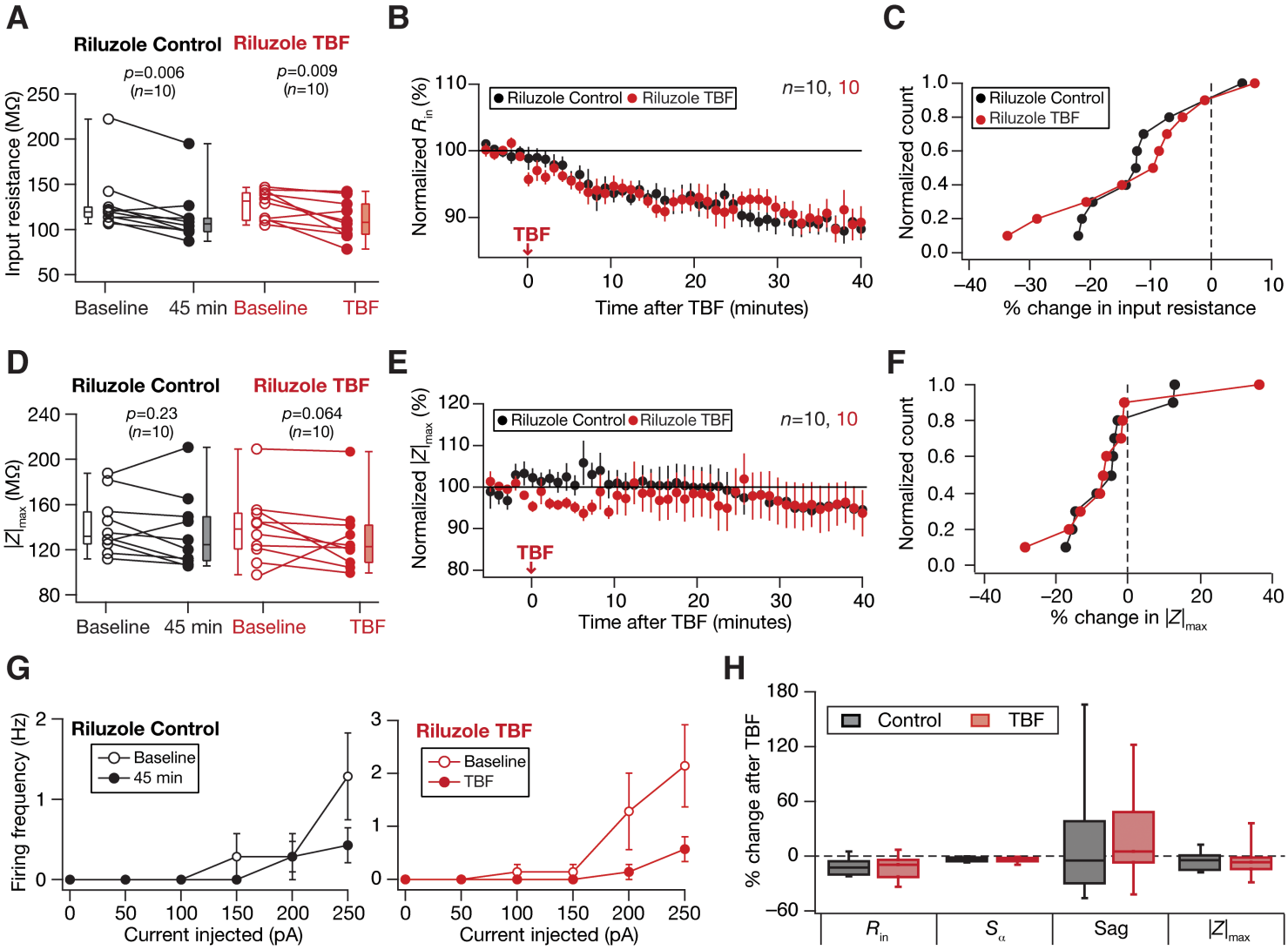

Mishra and Narayanan, Figure 7

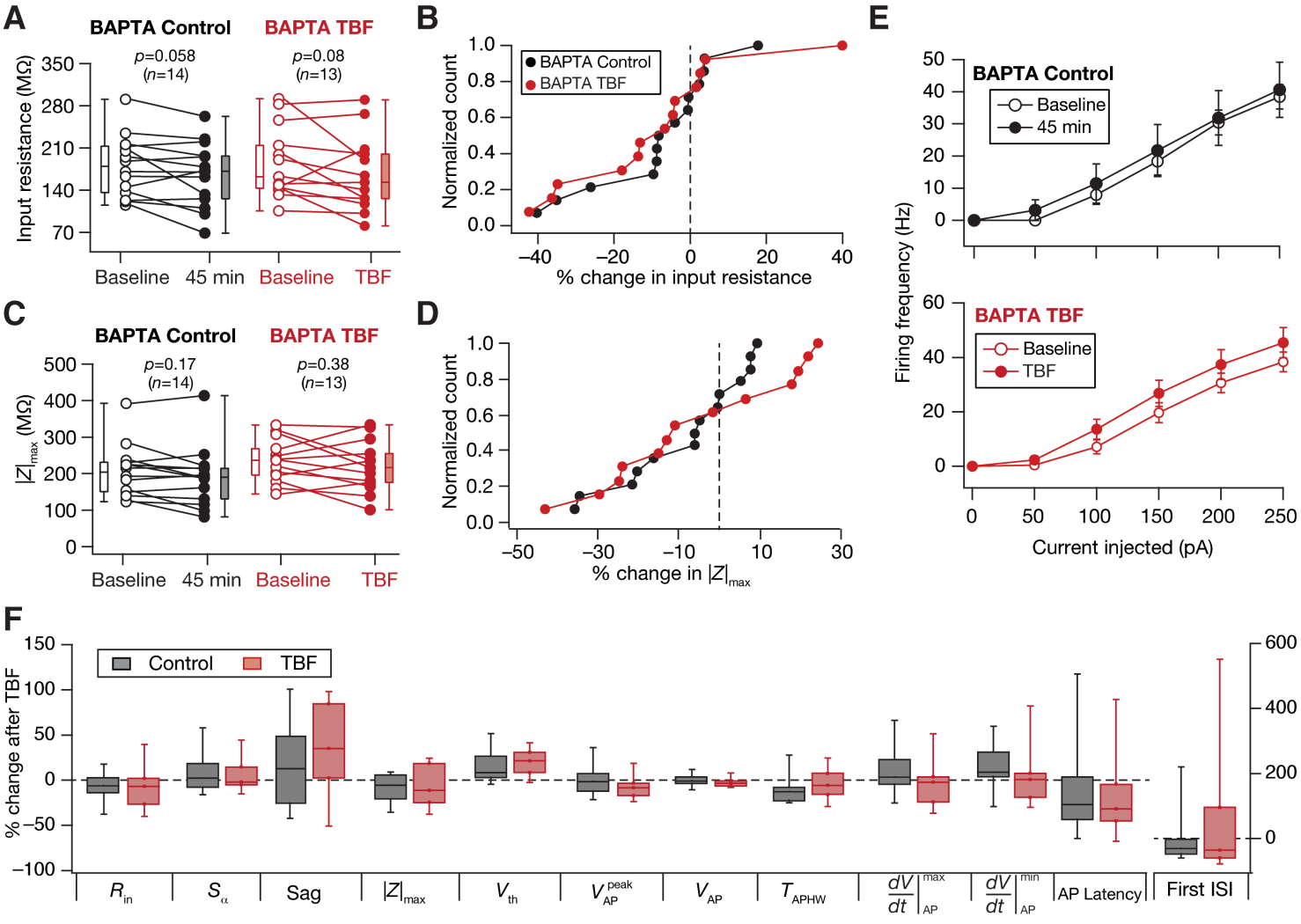

Mishra and Narayanan, Figure 8

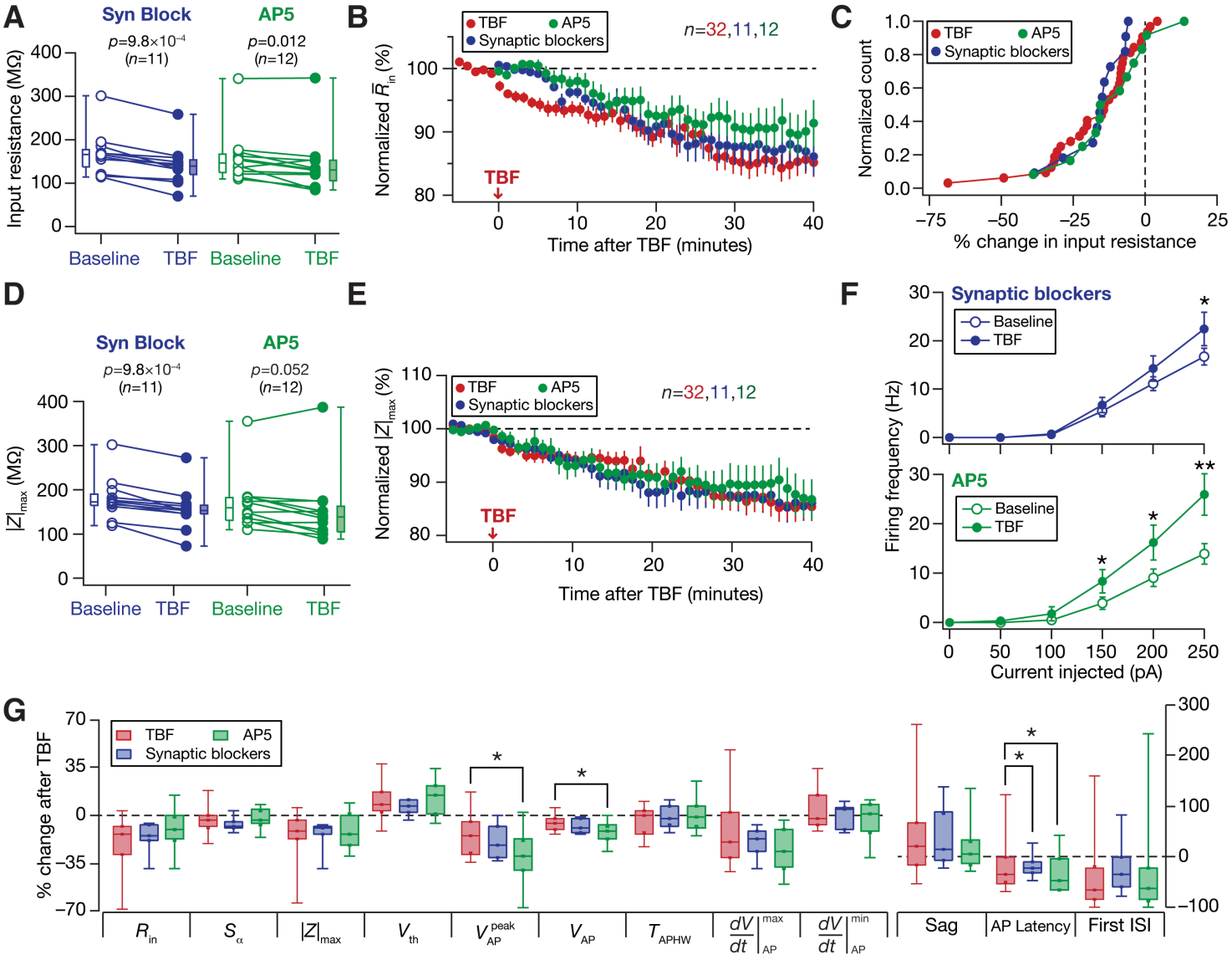

Mishra and Narayanan, Figure 9

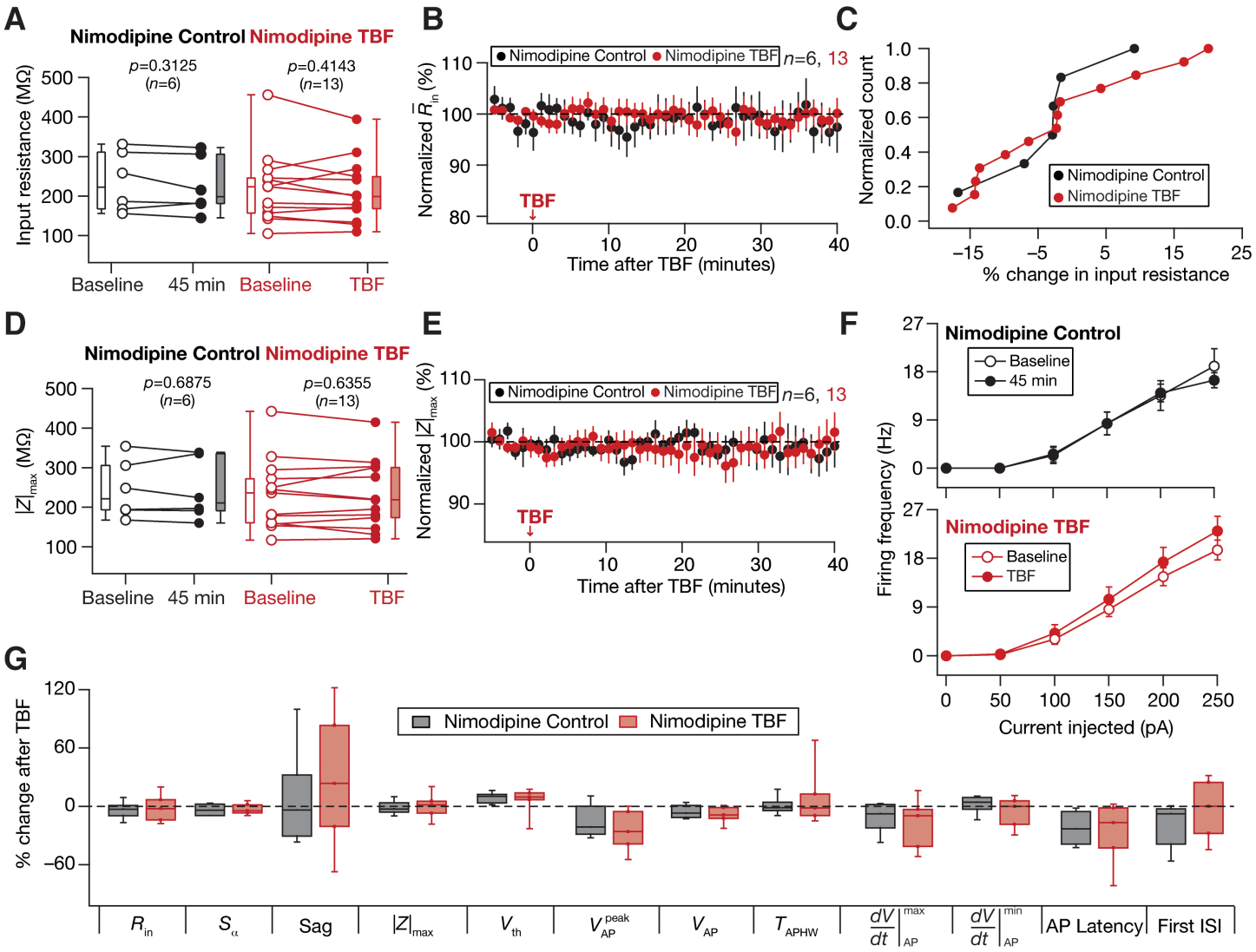

Mishra and Narayanan, Figure 10

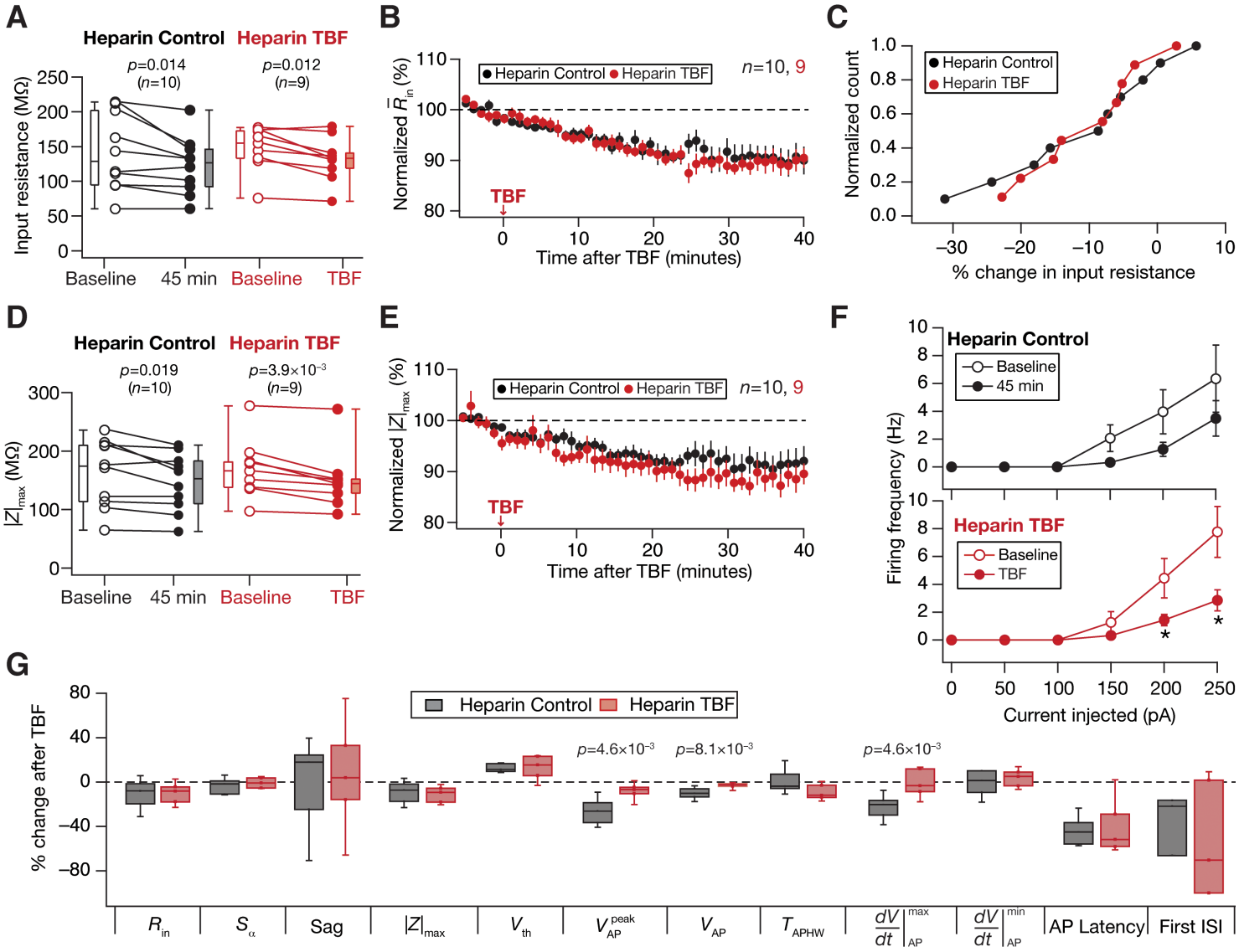

Mishra and Narayanan, Figure 11

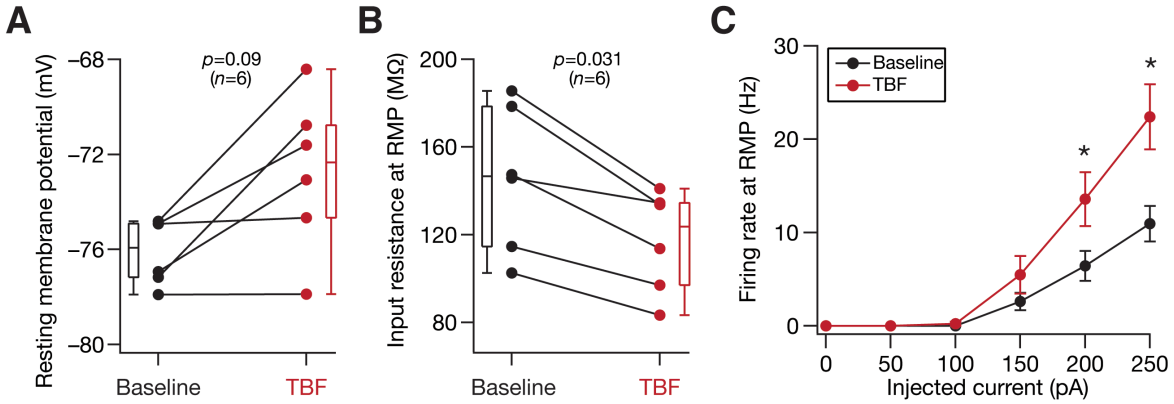

Mishra and Narayanan, Figure S1

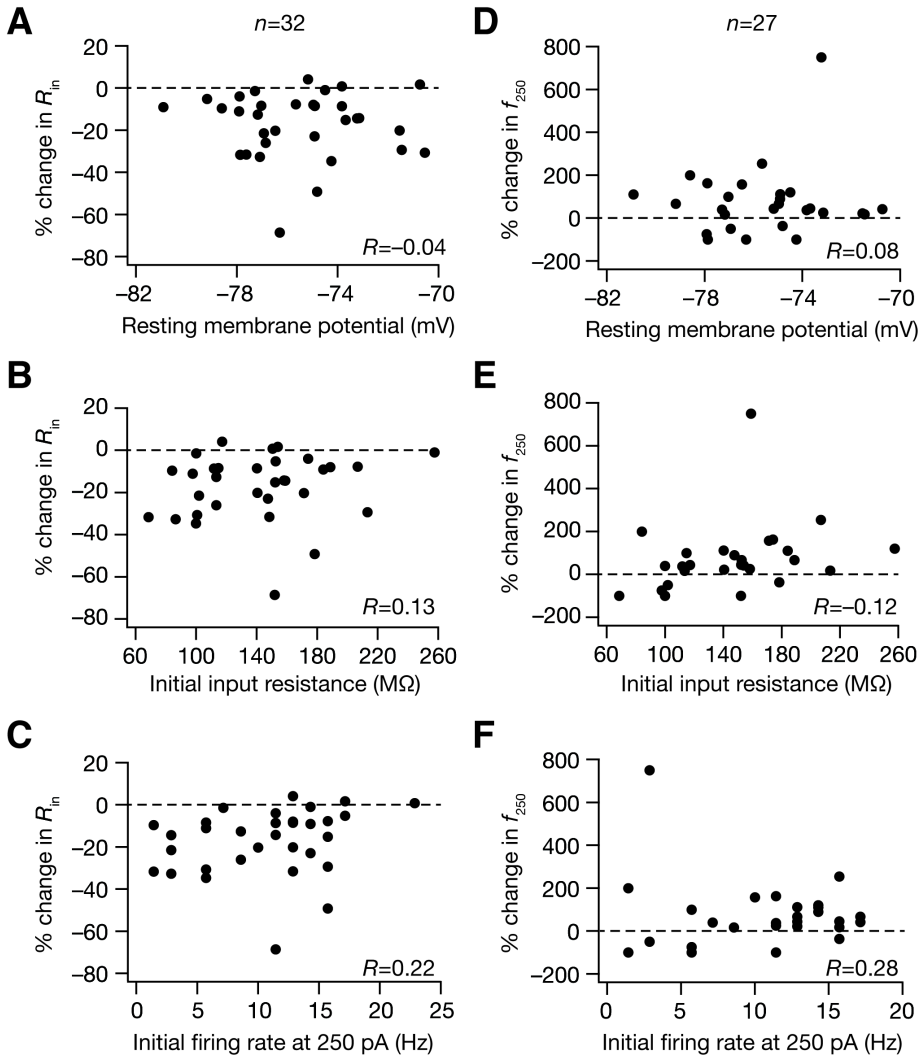

Mishra and Narayanan, Figure S2

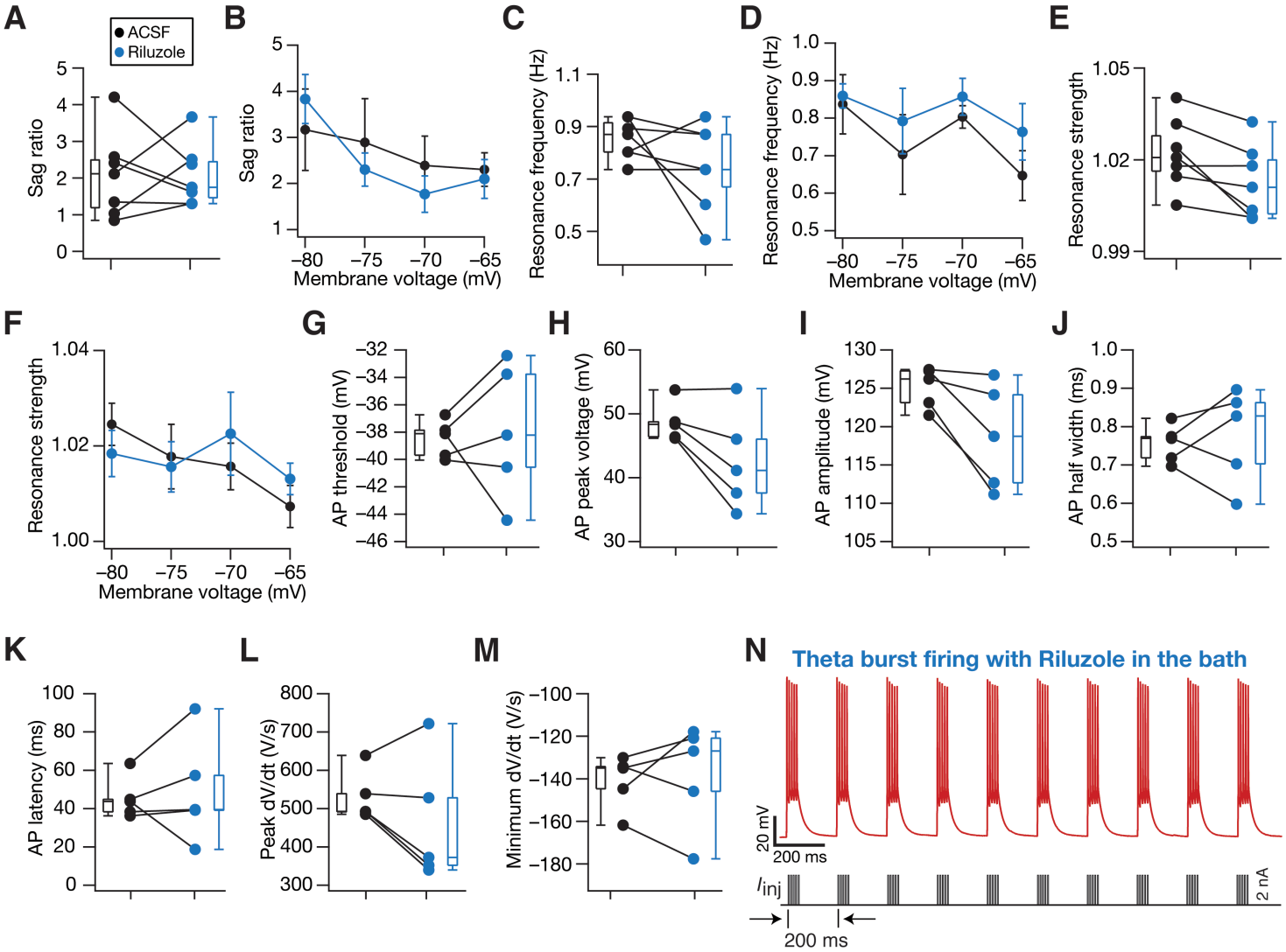

Mishra and Narayanan, Figure S3